The Biophysicist

Dynamical Models of Chemical Exchange in Nuclear Magnetic Resonance Spectroscopy

Nicolas Daffern[1], Christopher Nordyke[2], Meiling Zhang[3], Arthur G. Palmer III[4,*], John E. Straub[5,*]

[1]Department of Molecular Biosciences, Northwestern University, 4162 Cook Hall, Evanston, IL 60208, USA
[2]Department of Molecular, Cellular and Biomedical Sciences, University of New Hampshire, 46 College Road, Durham, NH 03824, USA
[3]Department of Chemistry and Biochemistry, University of Notre Dame, 236 Nieuwland Science Hall, Notre Dame, IN 46556, USA
[4]Department of Biochemistry and Molecular Biophysics, Columbia University, 630 West 168th Street, New York, NY 10032, USA
[5]Department of Chemistry, Boston University, 590 Commonwealth Avenue, Boston, MA 02215, USA

ABSTRACT Chemical exchange line broadening is an important phenomenon in nuclear magnetic resonance (NMR) spectroscopy, in which a nuclear spin experiences more than one magnetic environment as a result of chemical or conformational changes of a molecule. The dynamic process of chemical exchange strongly affects the sensitivity and resolution of NMR experiments and increasingly provides a powerful probe of the interconversion between chemical and conformational states of proteins, nucleic acids, and other biologic macromolecules. A simple and often used theoretic description of chemical exchange in NMR spectroscopy is based on an idealized 2-state jump model (the random phase or telegraph signal). However, chemical exchange can also be represented as a barrier crossing event that can be modeled by using chemical reaction rate theory. The timescale of crossing is determined by the barrier height, the temperature, and the dissipation modeled as collisional or frictional damping. This tutorial explores the connection between the NMR theory of chemical exchange line broadening and strong collision models for chemical kinetics in statistical mechanics. Theoretic modeling and numeric simulation are used to map the rate of barrier crossing dynamics of a particle on a potential energy surface to the chemical exchange relaxation rate constant. By developing explicit models for the exchange dynamics, the tutorial aims to elucidate the underlying dynamical processes that give rise to the rich phenomenology of chemical exchange observed in NMR spectroscopy. Software for generating and analyzing the numeric simulations is provided in the form of Python and Fortran source codes.

KEY WORDS barrier crossing dynamics; chemical kinetics; reaction rate theory; spin relaxation; strong collision model; computational modeling; fundamental concepts and techniques; tutorial

"*" corresponding authors

Received: 6 May 2021
Accepted: 17 September 2021
Published: 0 Month 2021

I. INTRODUCTION

Chemical exchange in nuclear magnetic resonance (NMR) spectroscopy describes the behavior of nuclear spins subject to stochastic fluctuations in the magnetic environments arising from transitions between in molecular chemical or conformational states. Chemical exchange provides insight into essential biomolecular dynamics

associated with critical events, such as protein and nucleic acid folding, ligand binding, allostery, and catalytic turnover (1–3). Developments in theoretic and experimental understanding of chemical exchange phenomena aids in the characterization of these biologic events by providing insight into the conformational dynamics of the underlying processes.

Various theoretic models have been developed to interpret chemical exchange (2). In each case, some underlying dynamical model is adopted that leads to time-dependent changes in the resonance frequency of the affected nuclear spin. The most popular models assume that dynamics consist of instantaneous jumps between 2 or more discrete states (4–6), although Schurr et al. considered a model with continuous Gaussian fluctuations in resonance frequency (7). Although the frequency associated with each state is unchanged by jumps, the time series is interrupted, leading to a decorrelation in time. This type of discontinuous jump model, sometimes referred to as a random phase model or telegraph signal, captures long timescale decorrelation but fails to account for shorter timescale dynamical fluctuations that may involve state-to-state transitions.

Chemical exchange leads to changes in resonance frequencies and relaxation rate constants of affected nuclear spins and hence to NMR resonance line shapes. In the simple 2-state telegraph model, a single nuclear spin exchanges between states with different resonance frequencies ω_1 and ω_2, with $\Delta\omega = \omega_2 - \omega_1$, according to the kinetic scheme:

$$A_1 \underset{k_{-1}}{\overset{k_1}{\rightleftharpoons}} A_2$$

in which $k_{ex} = k_1 + k_{-1}$ is the sum of the forward and reverse kinetic rate constants and the equilibrium populations of the 2 states are $p_1 = k_{-1}/k_{ex}$ and $p_2 = k_1/k_{ex}$, and $p_1 + p_2 = 1$. Stochastic changes in resonance frequencies, arising from transitions between the 2 states, lead to dephasing of components of the spin magnetization perpendicular to the static magnetic field. This results in shifts in resonance frequencies and additional contributions to transverse relaxation (with rate constant $R_2 = 1/T_2$). The NMR spectrum resulting from the chemical exchange process can be calculated from the Bloch–McConnell equations (1). Illustrative spectra for $p_1 = 0.8$, $p_2 = 0.2$, and $\Delta\omega = 1{,}000\ s^{-1}$ for different values of k_{ex} are shown in Figure 1.

In the absence of chemical exchange, individual resonance lines are observed at the frequencies ω_1 and ω_2, with integrated intensities proportional to p_1 and p_2 (not shown). When chemical exchange is slow on the NMR chemical shift timescale, $k_{ex} < \Delta\omega$, resolved resonance lines are still observed. However, the linewidths are increased because the transitions between states increase transverse relaxation rate constants. If the site populations are unequal with $p_1 > p_2$, then $k_{-1} > k_1$, and the resonance line for the minor population is preferentially broadened. In intermediate exchange or coalescence, $k_{ex} \approx \Delta\omega$, and a single very broad and shifted resonance line results, in many cases broadened to be unobservable in practice. In fast exchange, $k_{ex} > \Delta\omega$, and a single resonance line is observed at the population-averaged resonance frequency with a linewidth that becomes smaller as k_{ex} becomes even larger. The reduction in linewidth, or transverse relaxation rate constant, as k_{ex} increases in the fast exchange limit is called motional narrowing (vide infra). As illustrated by this simple example, the dramatic effects of the chemical kinetic process on the NMR line shapes, or equivalently resonance frequencies and transverse relaxation rate constants, is the basis for investigating chemical or conformational kinetic processes in biologic macromolecules.

As an intrinsic physical phenomenon, chemical exchange as evidenced in NMR spectroscopy must comply with physical kinetic theories of chemical reactions. To broaden the interdisciplinary understanding of chemical exchange, the present tutorial reviews statistical mechanical theories of chemical kinetics relevant to the modeling and interpretation of the phenomenon of chemical exchange in NMR spectroscopy. By mapping the chemical exchange phenomenon onto the dynamics of a particle moving stochastically in a classical

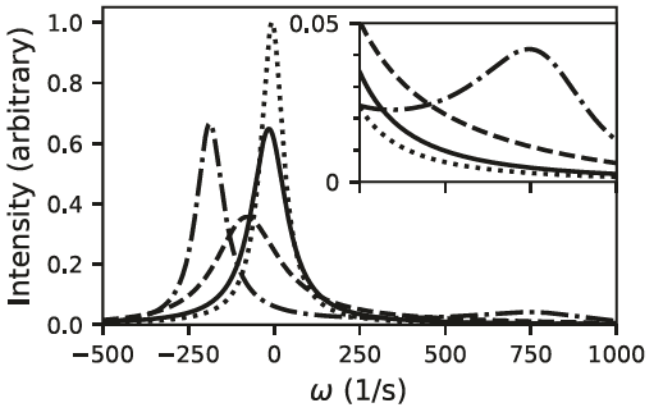

Fig 1. NMR spectra for 2-site chemical exchange. Parameters were $p_1 = 0.8$, $p_2 = 0.2$, $\omega_1 = -200$ s^{-1}, $\omega_2 = 800$ s^{-1}, and $\Delta\omega = 1{,}000$ s^{-1}, yielding the average resonance frequency $p_1\omega_1 + p_2\omega_2 = 0$ for convenience. The values of k_{ex} are 250 s^{-1} (dash–dotted line), 1,000 s^{-1} (dashed line), 2,500 s^{-1} (solid line), and 4,000 s^{-1} (dotted line), corresponding to slow, intermediate, fast, and very fast exchange on the chemical shift timescale, respectively. The inset shows a vertical expansion of the region from 250 to 1,000 s^{-1}. The transverse relaxation rate constants obtained for the major peak in each spectrum by fitting a Lorentzian line shape function over the region −500 to 300 s^{-1} were 49.7, 113.8, 61.6, and 39.5 s^{-1}, respectively. Spectra were calculated from the Bloch–McConnell equations (1).

biphasic potential (8, 9), reaction rate theory and models of barrier crossing dynamics can be used to explore the microscopic exchange dynamics and interpret chemical exchange in terms of the underlying chemical dynamics.

In this tutorial, we use state-of-the-art theories for chemical dynamics to generalize jumplike models of chemical exchange to barrier crossing dynamics of a particle along a reaction coordinate. We demonstrate that the introduction of a continuously varying coordinate variable, as opposed to a set of discrete states, can capture not only the long time decorrelation associated with barrier crossing but also the shorter timescale transient dynamics, associated with fluctuations within potential energy wells. Stochastic evolution is described by the strong collision model. This model assumes that the state of the system is randomized upon each collision, in accord with the equilibrium distribution. Collisions occurs at a rate α, leading to an exponential distribution of collision times, and the average change in energy due to a collision is large compared with k_BT. The resulting detailed models are shown to be consistent with the predictions of standard discrete state jump models, while adding a higher degree of realism in the underlying dynamics. This tutorial serves to elucidate the underlying phenomenon of exchange by reducing the complexity of detailed computational simulations of proteins and other macromolecules to the essential dynamics that dictate the rate of chemical exchange (10, 11).

The tutorial is organized as follows. Theoretic models of chemical exchange are developed by proposing a mapping between changes in coordinates and changes in resonance frequencies. The resulting time-dependent frequencies are used to evaluate time correlation functions associated with NMR observables. The predictions of the theoretic expressions are compared with the results of numeric simulations for the dynamics of a continuously varying coordinate in a biphasic double-well potential. The dynamics are explored for a variety of parameterizations of the potential wells and as a function of the rate of collisions. In an extension of these results for chemical exchange, the models are used to simulate Carr–Purcell–Meiboom–Gill (CPMG) relaxation dispersion decay (2, 10). Finally, suggestions are made for generalizations of this work to more detailed models of chemical dynamics.

II. THEORY

We consider, as a minimal model of chemical exchange dynamics, a single nuclear spin whose state is defined by a coordinate variable $q(t)$ that depends on time. Changes in the variable $q(t)$ capture changes in the environment of the nucleus, reflecting changes in the chemical or conformational state of the system. The associated resonance frequency of the nucleus, $\omega(t)$, is a function of the state of the system so that $\omega(t) = \omega[q(t)]$. Without loss of generality, the NMR radio frequency carrier can be assumed to be on resonance with the ensemble average of $<\omega(t)>$ so that $<\omega(t)> = 0$ by construction. As a model of the exchange dynamics, we adopt a standard model of chemical reaction dynamics, involving transitions between 2 mechanically stable states in a double-well (biphasic) potential. In terms of this simple model, the dynamics of the resonance

frequency of the nuclear spin $\omega[q(t)]$ involves fluctuations within and between 2 basins. The rate of transition between states is a function of barrier height, temperature, and dissipation.

In the simplest case, $q(t)$ is a 2-state telegraph signal taking on values 0 and 1 so that $q(t) = 1$ if the spin is in state 1 with resonance frequency ω_1 and $q(t) = 0$, if the spin is in the state 2 with resonance frequency ω_2. Thus, the instantaneous resonance frequency is expressed as $\omega(t) = q(t)\omega_1 + (1 - q(t))\omega_2$. This is the 2-state jump model commonly encountered in the theory of NMR spectroscopy and illustrated in Figure 1 (1). In the 2-state jump model, every collision is a strong collision in which the system loses memory of its prior state. The effect of transitions between $q(t) = 1$ and $q(t) = 0$, representing frequency jumps between ω_1 and ω_2, can be determined by a variety of mathematical approaches (1, 2, 5). In the following, we adopt an alternative approach commonly used in reaction rate theory in which $q(t)$ is a continuous rather than discrete variable. This allows exploration of a wider variety of models and enables a more detailed analysis of the underlying system dynamics.

A. Strong collision dynamics in the discrete state jump model

As an introduction to the approach used in the tutorial, a connection is established between strong collision models for chemical dynamics and transverse spin relaxation arising from chemical exchange. The complex-valued time-domain NMR signal (omitting a number of constants of proportionality) for a single stochastic realization of the 2-state jump process (also called the telegraph process) is given by (5, 12)

$$\begin{aligned} s^+(t) &= \exp\left\{ i \int_0^t [q(t')\omega_1 + (1 - q(t'))\omega_2] dt' \right\} \\ &= \exp\left\{ -i\Delta\omega \int_0^t [q(t') - p_1] dt' \right\} \\ &= q(t) \exp\{-ip_2\Delta\omega t\} \\ &\quad + [1 - q(t)] \exp\{ip_1\Delta\omega t\} \end{aligned} \tag{1}$$

in which $s^{\pm}(t) = s_x(t) \pm is_y(t)$ and $s_x(t)$ and $s_y(t)$ are the quadrature components of the signal. The second equality is obtained by noting that $p_1 = <q(t)>$ is the equilibrium population of the state 1 and recalling that $\Delta\omega = \omega_2 - \omega_1$ and $<\omega(t)> = p_1\omega_1 + p_2\omega_2 = 0$. The third equality is obtained in the absence of state changes so that $q(t)$ is either 0 or 1 for a given member of the ensemble. The observable NMR signal is the average over the ensemble of realizations of the stochastic process and is denoted $<s^+>(t)$. The ensemble average of the third equality reduces to $<s^+>(t) = p_1 \exp(i\omega_1 t) + p_2 \exp(i\omega_2 t)$, as expected in the absence of state changes. The usual theoretic analysis of spin relaxation in NMR spectroscopy would proceed essentially by calculation of the ensemble average of the second line of Eq. 1 to obtain the ensemble average NMR signal, including exchange-broadening effects (vide infra) (1). Instead, herein, the autocorrelation function of the NMR signal is calculated as

$$\begin{aligned} C(\tau) &= \langle s^+(t) s^-(t + \tau) \rangle \\ &= \lim_{T \to \infty} \frac{1}{T} \int_0^T s^+(t) s^-(t + \tau) dt \end{aligned} \tag{2}$$

in which the second equality assumes the system dynamics are stationary and ergodic. The autocorrelation function of the NMR signal in the absence of state changes is given by

$$\begin{aligned} C(\tau) &= \Big\langle \left(q(t) e^{-ip_2\Delta\omega t} + [1 - q(t)] e^{ip_1\Delta\omega t} \right) \\ &\quad \times \Big(q(t + \tau) e^{ip_2\Delta\omega(t+\tau)} \\ &\quad + [1 - q(t + \tau)] e^{-ip_1\Delta\omega(t+\tau)} \Big) \Big\rangle \\ &= p_1 e^{ip_2\Delta\omega\tau} + p_2 e^{-ip_1\Delta\omega\tau} \end{aligned} \tag{3}$$

in which the third equality of Eq. 1 has been substituted into Eq. 3. The final result in Eq. 3 is obtained by noting that $q(t)^2 = q(t)$ and that in the absence of state changes, $q(t) = q(t+\tau)$. The Laplace transform of the resulting autocorrelation function is

$$C(s) = \int_0^\infty C(\tau) e^{-s\tau} d\tau = \frac{p_1}{s - ip_2\Delta\omega} + \frac{p_2}{s + ip_1\Delta\omega} \tag{4}$$

To proceed, $q(t)$ is assumed to be time dependent because strong collisions cause state-to-state transitions. A theorem from statistical mechanics states that the Laplace transform of the autocorrelation function of a dynamical system in the presence of strong collisions $\tilde{C}(s)$ is a function of the autocorrelation function in the absence of collisions $C(s)$ (8, 9):

$$\tilde{C}(s) = \frac{C(s+\alpha)}{1-\alpha C(s+\alpha)} \tag{5}$$

in which α is the collision rate. Substituting Eq. 4 into Eq. 5 gives

$$\tilde{C}(s) = \frac{s+\alpha-i\Delta\omega\Delta p}{s^2+\{\alpha-i\Delta\omega\Delta p\}s+p_1p_2\Delta\omega^2} \tag{6}$$

in which $\Delta p = p_2 - p_1$. Eq. 6 is the Laplace transform of the 2-state jump process in the strong collision model. The inverse Laplace transform of Eq. 6 yields the corresponding autocorrelation function in the time domain:

$$\begin{aligned}\tilde{C}(\tau) = e^{-(\alpha-i\Delta\omega\Delta p)\tau/2} &\left\{\cosh\left(\frac{\tau}{2}\sqrt{\alpha^2-\Delta\omega^2-2i\alpha\Delta\omega\Delta p}\right)\right.\\ &+\frac{\alpha-i\Delta\omega\Delta p}{\sqrt{\alpha^2-\Delta\omega^2-2i\alpha\Delta\omega\Delta p}}\\ &\left.\times\sinh\left(\frac{\tau}{2}\sqrt{\alpha^2-\Delta\omega^2-2i\alpha\Delta\omega\Delta p}\right)\right\}\end{aligned} \tag{7}$$

This equation is exact but is also complicated. Fortunately, useful limiting results can be obtained as described in the following.

When transitions between states are sufficiently fast, the transverse relaxation rate constant is given by the decay of the autocorrelation function at long times (after any initial transients have decayed to zero) (4, 6). This corresponds to the limit $s \to 0$ in the Laplace domain. The usefulness of the analysis in the Laplace domain is that the long time behavior is inferred from the small s limit, allowing relatively simple approximations to be applied.

To begin, Eq. 6 can be expressed as

$$\tilde{C}(s) = \frac{1}{s+\frac{p_1p_2\Delta\omega^2}{s+\alpha-i\Delta\omega\Delta p}} = \frac{1}{s+D(s)} \tag{8}$$

$D(s)$ can be expanded in a Taylor series as

$$D(s) \approx \frac{p_1p_2\Delta\omega^2}{\alpha-i\Delta\omega\Delta p} - s\frac{p_1p_2\Delta\omega^2}{(\alpha-i\Delta\omega\Delta p)^2} + \ldots \tag{9}$$

Keeping only the first 2 terms of the series, Eq. 8 becomes

$$\begin{aligned}\tilde{C}(s) &= \frac{1}{s\left(1-\frac{p_1p_2\Delta\omega^2}{(\alpha-i\Delta\omega\Delta p)^2}\right)+\frac{p_1p_2\Delta\omega^2}{\alpha-i\Delta\omega\Delta p}}\\ &= \frac{\left(1-\frac{p_1p_2\Delta\omega^2}{(\alpha-1\Delta\omega\Delta p)^2}\right)^{-1}}{s+\left(1-\frac{p_1p_2\Delta\omega^2}{(\alpha-1\Delta\omega\Delta p)^2}\right)^{-1}\frac{p_1p_2\Delta\omega^2}{\alpha-1\Delta\omega\Delta p}}\end{aligned} \tag{10}$$

This equation is isomorphic to a result derived from the Bloch–McConnell equations by Abergel and Palmer (Eq. 23 in (13)). The second equality of Eq. 10 is the Laplace transform of $\tilde{C}(\tau) = Ae^{i\phi}\exp[(i\Omega_{sc}-R_{sc})\tau]$ in which

$$\begin{aligned}a &= \left|\left(1-\frac{p_1p_2\Delta\omega^2}{(\alpha-i\Delta\omega\Delta p)^2}\right)^{-1}\right|\\ \phi &= \mathrm{Arg}\left[\left(1-\frac{p_1p_2\Delta\omega^2}{(\alpha-i\Delta\omega\Delta p)^2}\right)^{-1}\right]\\ \Omega_{sc} &= \mathrm{Im}\left[\left(1-\frac{p_1p_2\Delta\omega^2}{(\alpha-i\Delta\omega\Delta p)^2}\right)^{-1}\frac{p_1p_2\Delta\omega^2}{\alpha-i\Delta\omega\Delta p}\right]\\ R_{sc} &= \mathrm{Re}\left[\left(1-\frac{p_1p_2\Delta\omega^2}{(\alpha-i\Delta\omega\Delta p)^2}\right)^{-1}\frac{p_1p_2\Delta\omega^2}{\alpha-i\Delta\omega\Delta p}\right]\end{aligned} \tag{12}$$

a and ϕ are the amplitude and phase of the long time component of the autocorrelation function, Ω_{sc} is the resonance frequency, and R_{sc} is the transverse relaxation rate constant in the 2-state strong collision model. Following the procedure of Abergel and Palmer yields an explicit form for R_{sc} (Eq. 31 in (13)):

$$\begin{aligned}R_{sc} &= p_1p_2\Delta\omega^2\alpha\\ &\times\left[\frac{\alpha^2+\Delta\omega^2}{(\alpha^2+\Delta\omega^2)^2-p_1p_2(5\alpha^2+\Delta\omega^2)\Delta\omega^2}\right]\end{aligned} \tag{13}$$

(a related expression for Ω_{sc} is given by Eq. 32 in (13) but not needed in this tutorial).

If collisions are in the fast limit on the NMR chemical shift timescale, $\alpha >> \Delta\omega$, then the bracketed term in Eq. 13 approaches α^{-2} and

$$R_{sc} = p_1 p_2 \Delta\omega^2/\alpha \qquad (14)$$

Eq. 14 also can be obtained in straightforward fashion by retaining only the first term in the series in Eq. 9 and assuming $\alpha >> \Delta\omega$. These results demonstrate that the autocorrelation function of the NMR signal in the fast limit strong collision 2-state telegraph model is a single exponential decay with rate constant R_{sc}. For comparison, either the random phase model or Bloch-Wangsness-Redfield (BWR) theory applied to the ensemble average of the second line of Eq. 1 give the fast limit expression for R_{BWR} as the integral of the autocorrelation function for the resonance frequency fluctuations $C(\tau) = <\delta\omega(t)\ \delta\omega(t+\tau)>$ (1, 5), in which $\delta\omega(t) = \omega(t) - <\omega(t)>$ is the instantaneous resonance frequency fluctuation. For the 2-state telegraph process, $C(\tau) = p_1 p_2 \Delta\omega^2 \exp(-k_{ex}\tau)$, in which $\delta\omega(t) = -\Delta\omega[q(t) - p_1]$ and $C(0) = \langle\delta\omega^2(t)\rangle = p_1 p_2 \Delta\omega^2$, yielding:

$$R_{BWR} = \int_0^\infty \langle\delta\omega(t)\delta\omega(t+\tau)\rangle d\tau = p_1 p_2 \Delta\omega^2/k_{ex} \qquad (15)$$

Eqs. 14 and 15 identify the collision rate α as being equal to the exchange rate k_{ex}. This casts the strong collision relaxation rate constant in the familiar form used in NMR spectroscopy. In statistical mechanics, a strong collision imparts variation in particle energy in the order of $k_B T$. In contrast, in NMR spectroscopy, only collisions that lead to changes in resonance frequency contribute to relaxation properties of the affected nuclear spin. That is, only the fraction of "collisions" that lead to transitions between states with different resonance frequencies are meaningful for spin relaxation. For the 2-state telegraph model, k_{ex} is the only nonzero eigenvalue of the kinetic transition matrix and consequently the only rate constant appearing in Eq. 15, and by extension, Eqs. 13 and 14. Eqs. 14 and 15 also provide an important identity between the (slow) long time decay of the NMR signal and the autocorrelation function of the (fast) resonance frequency fluctuations in the fast (or BWR) limit.

Figure 2 compares the results for the strong collision autocorrelation function calculated from Eq. 7 and the single exponential approximations with rate constants given by Eqs. 13 and 14. When $\alpha < \Delta\omega$, the imaginary component of the exact autocorrelation function is large and the fast limit (or BWR) approximation of Eq. 14 is not accurate (Fig 2a,b). As α increases so that $\alpha > \Delta\omega$, the imaginary component of the autocorrelation function decreases in magnitude and the fast limit approximation becomes increasingly accurate (Fig 2c,d). When $\alpha > 4\Delta\omega$, the exact autocorrelation function becomes nearly real, and the fast limit approximation is nearly exact (Fig 2d). The extended formula for R_{sc} in Eq. 13 is accurate for intermediate (Fig 2b) and slow exchange for times τ longer than approximately (4–5)/α, after the initial fast decay of the autocorrelation function (Fig 2a), as well as fast exchange (Fig 2c,d). For the given illustrative parameters, Eq. 13 underestimates the relaxation rate constant obtained from line shape fitting by a maximum of 7.5% for intermediate exchange and becomes highly accurate in the fast exchange regime (see Figs 1 and 2 captions). The remainder of the tutorial focuses for simplicity on the fast limit regime for simplicity, but as indicated by Eq. 13 and the results in Figure 2, the approaches developed are more generally applicable outside this limit.

Additional details regarding the Laplace transform approach used to determine theoretic expressions for NMR spin relaxation rate constants are provided elsewhere (4–6, 13). A similar strong collision model has been applied to model the free induction decay, corresponding to $<s^+>(t)$, in NMR spectroscopy by Goldman and Goldman et al. (12, 14).

B. Strong collision dynamics in the continuous reaction coordinate model

In the 2-state jump model discussed previously, the states of the system are discrete, and

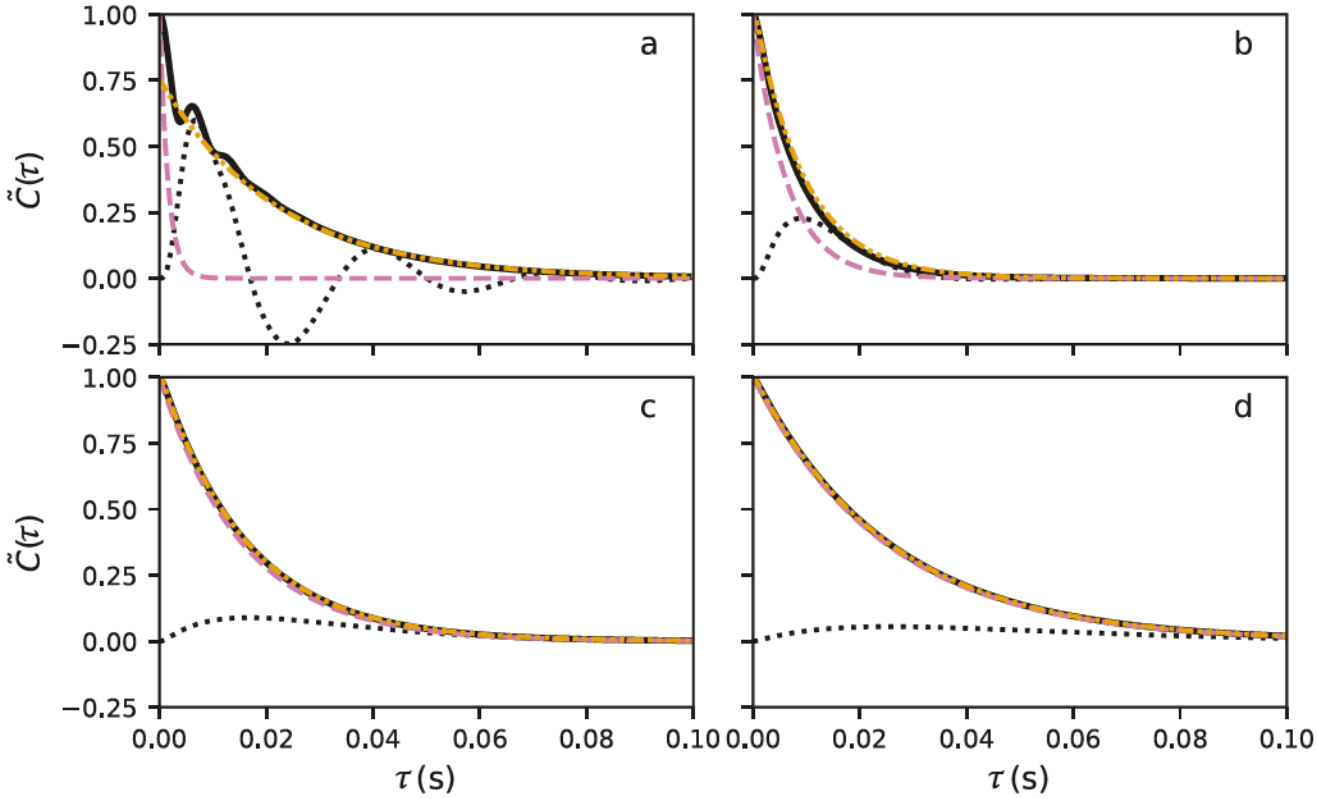

Fig 2. Comparison of exact autocorrelation functions for the strong collision model and single exponential approximations. Parameters were $p_1 = 0.8$, $p_2 = 0.2$, and $\Delta\omega = 1{,}000\ s^{-1}$, and α varied between (a) $250\ s^{-1}$, (b) $1{,}000\ s^{-1}$, (c) $2{,}500\ s^{-1}$, and (d) $4{,}000\ s^{-1}$ (identical to Fig 1). Plots show the magnitudes of the real (solid, black lines) and imaginary (dotted, black lines) components of the exact complex autocorrelation function calculated from Eq. 7; the fast limit single exponential approximation of Eq. 14 (dashed, reddish–purple lines); and the single exponential approximation of Eq. 13 with amplitude A, given by Eq. 12 (dash–dot–dotted, orange lines). The relaxation rate constants calculated from Eq. 13 are 46.2, 105.3, 61.2, and 39.4 for Fig. 2a–d, respectively, and are 7.0%, 7.5%, 0.6%, and 0.1%, smaller than the values obtained from fitting the corresponding NMR spectra (Fig 1).

the coordinate variable $q(t)$ is restricted to values of 0 and 1. This is essentially a square-well model, in which each well is associated with a unique resonance frequency and the transit time across the barrier between wells is short compared with residence times within the wells. A more realistic model of the chemical dynamics uses a continuous positional variable $q(t)$ moving in a double-well (biphasic A–B) potential. The continuous dependence of the variable $q(t)$ provides a more realistic model for classical reaction dynamics. We use the double-well potential function (8)

$$V(q) = \left\{ \begin{array}{cc} \frac{1}{2}m\omega_A^2(q+q_A)^2 & q < -a \\ Q - \frac{1}{2}m\omega_1^2 q^2 & -a \leqslant q < b \\ V_B + \frac{1}{2}m\omega_B^2(q-q_B)^2 & q \geq b \end{array} \right\} \tag{16}$$

in which Q is the energy barrier height between wells, V_B is the difference in energy between the well A and B minima, q_A and q_B are the positions of the well minima, m is the particle mass, and ω_1 is the barrier transition frequency (note that the frequency parameters here are constants and are distinct from time-dependent NMR resonance frequency $\omega(t)$). These parameters are specified to set the shape of the potential, and the definitions

$$\begin{aligned} a &= 2Q/(m\omega_1^2 q_A) \\ b &= 2(Q - V_B)/(m\omega_1^2 q_B) \\ \omega_A &= \omega_1\sqrt{a/(q_A - a)} \\ \omega_B &= \omega_1\sqrt{b/(q_B - b)} \end{aligned} \tag{17}$$

ensure that $V(q)$ and $dV(q)/dq$ are continuous. The potential can be recast in dimensionless variables:

$$\hat{V}(\hat{q}) = \begin{Bmatrix} \frac{1}{2}\hat{\omega}_A^2(\hat{q}+\hat{q}_A)^2 & \hat{q} < -\hat{a} \\ \hat{Q} - \frac{1}{2}\hat{q}^2 & -\hat{a} \leq \hat{q} < \hat{b} \\ \hat{V}_B + \frac{1}{2}\hat{\omega}_B^2(\hat{q}-\hat{q}_B)^2 & \hat{q} \geq \hat{b} \end{Bmatrix} \tag{18}$$

in which energy variables $\hat{V}_B = V_B/(k_BT)$ and $\hat{Q} = Q/(k_BT)$ are in units of k_BT, length variables are redefined as $\hat{x} = [m\omega_1^2/(k_BT)]^{1/2}x$ for $x = \{q, q_A, q_B, a, b\}$, and frequency variables are redefined as $\hat{\omega}_\gamma = \omega_\gamma/\omega_1$ for $\gamma = \{1, A, B\}$. Dimensionless time variables are defined as $\hat{t} = \omega_1 t$, and the dimensionless collision rate is $\hat{a} = \alpha/\omega_1$ (vide infra). For convenience, the circumflex will be omitted in the following discussion, but all variables should be regarded as dimensionless, unless otherwise noted. Examples of the potential are shown in Figure 3. In the following, populations of sites 1 and 2 were obtained by integrating the canonical ensemble probability, assuming $q < 0$ corresponds to site 1 and $q > 0$ corresponds to site 2.

III. METHODS

The stepwise procedure followed in modeling strong collision dynamics is provided alongside the algorithm used to conduct the simulations. The mapping of the simple dynamical model to actual physical systems is discussed, including the particular example of protein folding. The use of the dynamical model to describe signal decay in a CPMG experiment is discussed.

A. Simulations for strong collisions

The previous theoretic discussion suggests a simple strategy for simulating chemical exchange dynamics by using the biphasic potential model:

(a) Generate a simulation of $q(t) = q(t_n) = q(n\Delta t) = q_n$ for a particle in the biphasic potential in the absence of collisions by solving Newton equations of motion for a series of time steps $n = \{0,\ldots, n_{max} - 1\}$ with duration Δt. In the present work, the velocity Verlet algorithm was used for propagating $q(t)$ and the velocity $v(t)$.

(b) Add strong collisions that occur in time with an exponential probability distribution. Each collision randomly reassigns the particle velocity from a Gaussian distribution centered at zero with variance $<v^2> = k_BT/m$ ($= 1$ in dimensionless units).

(c) Map from $q(t)$ to $\omega[q(t)] = \omega(t)$.

(d) Calculate the autocorrelation function of $\delta\omega(t)$, given by $<\delta\omega(t)\delta\omega(t+\tau)>$.

(e) Calculate the autocorrelation function for $s^{\pm}(t)$ by using Eq. 2 and the definition:

$$s^{\pm}(t) = s^{\pm}(n\Delta t) = \exp\left(\pm i\Delta t \sum_{k=0}^{n} \omega_k\right)$$

(f) Calculate the ensemble average NMR signal $<s^+>(t)$ by averaging $s^+(t)$ over multiple independent trajectories, $q(t)$.

The finite difference equations of motion for the coordinate variable $q(t)$ and the velocity $v(t)$ are defined by the velocity Verlet algorithm (in dimensionless units):

$$\begin{aligned} q(t+\Delta t) &= q(t) + v(t)\Delta t + \frac{F(t)}{2}\Delta t^2 \\ v(t+\Delta t) &= v(t) + \frac{F(t+\Delta t) + F(t)}{2}\Delta t \end{aligned} \tag{19}$$

in which the dimensionless instantaneous acceleration of a particle at a particular position q is given by

$$\begin{aligned} F(q) &= -\frac{dV(q)}{dq} \\ &= \begin{Bmatrix} -\omega_A^2(q-q_A) & q < -a \\ q & -a \leq q < b \\ -\omega_B^2(q-q_B) & q \geq b \end{Bmatrix} \end{aligned} \tag{20}$$

Python code illustrating the simulation algorithm is shown in Box 1. Autocorrelation functions can be calculated by approximations of the integral in Eq. 2 through a summation (substituting $\delta\omega(t)$ for $s^+(t)$ as needed) or more efficiently by Fourier transformation.

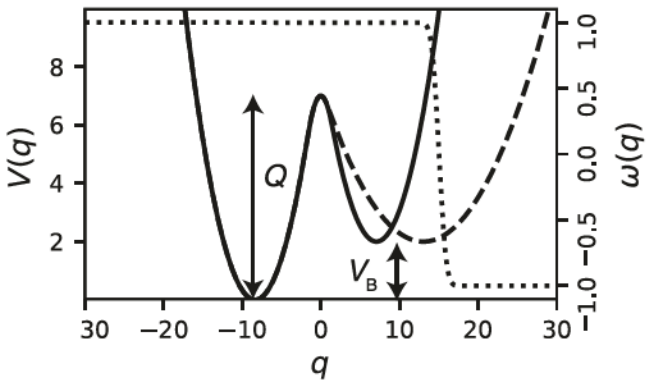

Fig 3. Biphasic potential calculated from Eqs. 17 and 18. Parameters (solid) are $Q = 7$, $V_B = 2$, and $\omega_A = \omega_B = 0.5$ yield $q_A = 8.37$, $q_B = 7.07$, $a = 1.67$, and $b = 1.41$. Parameters (dashed) $Q = 7$, $V_B = 2$, $\omega_A = 0.5$, and $\omega_B = 0.25$ yield $q_A = 8.37$, $q_B = 13.04$, $a = 1.67$, and $b = 0.77$. Chemical shift profile $\omega(q)$ for the random-coil model adapted to (dashed) asymmetric potential (dotted). The Boltzmann-weighted average $<\omega(q)> = 0$ for $q > 0$. All parameters are dimensionless, as described in the text.

B. Mapping generalized coordinates to resonance frequencies

The mapping of the coordinate variable $q(t)$ to the resonance frequency $\omega(t)$ was performed in 2 ways. In the first approach, a resonance frequency of 1 was assigned, if $q < 0$, and a resonance frequency of 0 was assigned, if $q \geq 0$. The values of the resonance frequencies were then shifted and scaled so that $<\omega(t)> = 0$ and $<\omega(t)^2>^{1/2} \tau_c = 0.1$ in which τ_c is the long time decay time for the autocorrelation function of $q(t)$. The latter constraint ensures that the NMR fast exchange limit is reached. This mapping reduces the simulated model to the 2-state telegraph jump process analyzed theoretically, as mentioned previously.

In the second approach, the chemical shifts were modeled initially by using $\omega(q) = -\text{erf}(q - q_0)$ in which erf is the error function. The value of q_0 is chosen so that $\omega(q) \approx 1$ for $q < 0$ and $\omega(q)$ varies between $+1$ and -1, with $<\omega(q)> \approx 0$ for $q \geq 0$, as illustrated in Figure 3. This function was then shifted and scaled so that $<\omega(t)> = 0$ and $<\omega(t)^2>^{1/2} \tau_c = 0.1$, as for the first approach. This second approach is a simple model of a major state 1 with a fixed resonance frequency (such as would occur in a folded state of a protein) and a minor state 2 in which local conformational fluctuations drive concomitant time-dependent variations in resonance frequencies. This mapping will be called the random-coil model in the following.

To illustrate the previous models, the $^{13}C\alpha$ spin has a secondary chemical shift, $\Delta\delta$, of 2 to 4 ppm in the α-helical conformation of a protein. The secondary shift is defined as the measured chemical shift minus the chemical shift expected for an unstructured (random-coil) peptide. Thus, the telegraph model assigns a single frequency equal to $\Delta\delta$ in the folded state and a single frequency equal to 0 in the unfolded state. The random-coil model also assigns a single frequency equal to $\Delta\delta$ in the folded state. However, the unfolded state is described by a fluctuating distribution of frequencies from $-\Delta\delta$ to $+\Delta\delta$, with an average of 0, representing in a simple manner the averaging of chemical shifts over the distributions of conformations sampled by a disordered peptide.

C. CPMG relaxation dispersion

CPMG and $R_{1\rho}$ relaxation dispersion experiments have developed as powerful approaches for investigation of microsecond to millisecond timescale dynamic processes in proteins and other macromolecules (2). In the CPMG experiment, relaxation is measured during a train of spin–echo sequences: $(\tau_{cp} - 180^\circ - \tau_{cp})_n$, in which 180° is a radiofrequency refocusing pulse, τ_{cp} is the spin–echo delay time, the total relaxation delay period is $T = 2n\tau_{cp}$, and n is the number of spin–echo units applied. In the ideal case, each 180° pulse merely acts to invert the sign of the evolution frequencies. As such, in the previous protocols, the effect of a CPMG pulse train is modeled by multiplying $\omega(t)$ by a square wave varying between $+1$ and -1, with 50% duty cycle and period $4\tau_{cp}$, prior to further analysis of $\omega(t)$. The autocorrelation function of $s^+(t)$ is calculated as described previously, or an ensemble average $<s^+>(t)$ is estimated by averaging multiple stochastic trajectories to mimic the signal decay in an actual CPMG experiment.

The variation in the observed relaxation rate as a function of the pulse delay τ_{cp} is called a

Box 1. Algorithm for strong collisions

```
dt = value                # time step
alpha = value             # collision rate
cut = np.exp(-alpha*dt) # test statistic for collisions
nsteps = value            # number of simulation steps
q = numpy.zeros(nsteps) # position trajectory
v = numpy.zeros(nsteps) # velocity trajectory
sigv = 1                  # standard deviation of velocity
q[0] = -qA                # initial position
v[0] = numpy.random.normal(0,sigv,1)     # initial velocity
F0 = Fq(q0,Q,VB,qA,qB)  # subroutine to calculate acceleration
for i in range(1,nsteps):                  # main loop
  q[i] = q[i-1] + v[i-1]*dt + F0*dt**2/2  # update position
  F1 = Fq(q[i],Q,VB,qA,qB)                 # update acceleration
  v[i] = v[i-1] + (F1+F0)*dt/2             # update velocity
  F0 = F1                                  # current acceleration
  if (numpy.random.random(1) > cut):       # test for collision
    v[i] = numpy.random.normal(0,sigv,1)  # randomize velocity
```

CPMG relaxation dispersion curve. In the fast exchange limit, analysis of the relaxation dispersion curve for a 2-state model yields

$$R_{CPMG}(\tau_{cp}) = p_1 p_2 \Delta\omega^2 \tau_{ex}\left[1 - \frac{\tau_{ex}}{\tau_{cp}}\tanh\left(\frac{\tau_{cp}}{\tau_{ex}}\right)\right] \quad (21)$$

in which the exchange time $\tau_{ex} = 1/k_{ex}$. More complex expressions for $R_{CPMG}(\tau_{cp})$, valid for all chemical exchange timescales, have been reported and widely used in the analysis of experimental data (2).

IV. RESULTS

Strong collision simulations were performed by using in-house Python version 3.6 (Python Software Foundation, Beaverton, OR) or GNU Fortran version 5.2.0 (Free Software Foundation, Inc., Boston, MA) programs; equivalent results were obtained with either programming language (but the Fortran routine is much faster). Numeric and graphic analyses of simulation trajectories were performed by using in-house Python 3.6 programs. The Python and

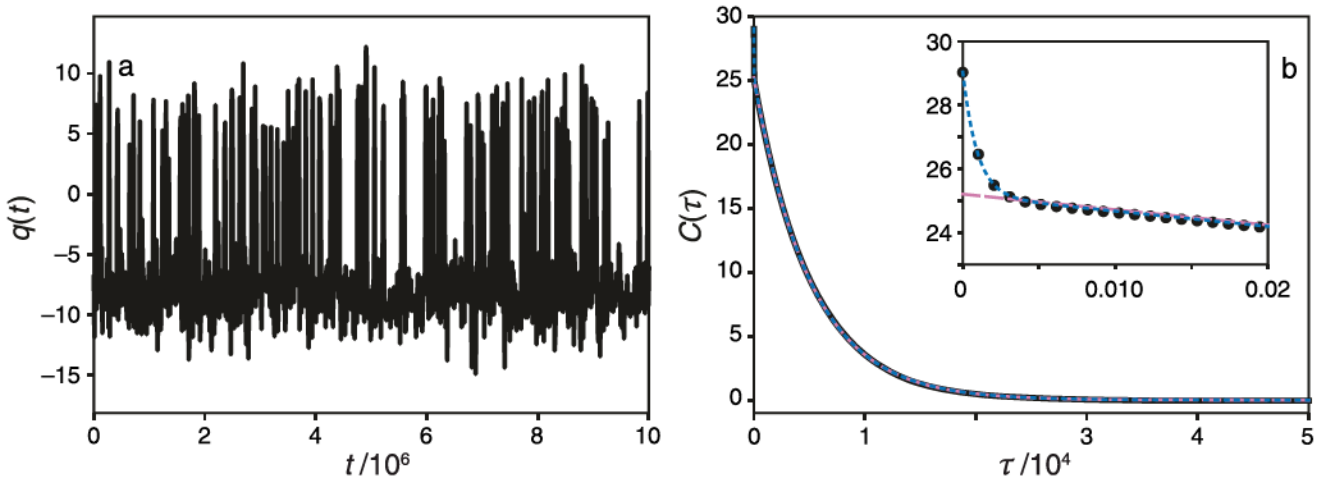

Fig 4. Simulation for the strong collision dynamics of the coordinate $q(t)$ in a biphasic double-well potential with $Q = 7$, $V_B = 2$, and equal well frequencies $\omega_A = \omega_B = 0.5$. (solid trace in Fig 2). The simulation used a time step of 0.01 and consisted of 2^{34} steps with a collision rate of $\alpha = 2.5$; $q(t)$ was stored every 2^{10} steps. (a) $q(t)$ at every 1,000 stored sample point during the simulation. (b) Autocorrelation function $C(\tau)$ of $q(t)$ (black) fit with a monoexponential (reddish–purple, dashed line) and biexponential decay function (blue, dotted line); 10 replicate simulations were averaged to produce the final autocorrelation function. The inset shows the fast initial decay of the autocorrelation function, which is well described by the biexponential fit. The fitted parameters are amplitudes $a_1 = 3.9$ and $a_2 = 25.2$ and decay times $\tau_1 = 9.4$ and $\tau_2 = 5{,}110$, respectively. All parameters are dimensionless as described in the text. The simulated dynamics in the potential are shown in Supplemental Movie S1.

Fortran programs used in this tutorial are provided in the Supplemental Material.

A. Strong collision dynamics in the biphasic potential

Initial simulations were performed by using parameters $Q = 7$, $V_B = 2$, and $\omega_A = \omega_B = 0.5$ (solid curve in Fig 3). The site populations are $p_1 = 0.88$ and $p_2 = 0.12$. Simulations were performed by using values of collision rate α, ranging between 10^{-3} and 10^2. Dynamics were underdamped for $\alpha < 0.3$ and overdamped otherwise. The simulated time series for the coordinate variable $q(t)$ and the autocorrelation function of $q(t)$ for the simulation with $\alpha = 2.5$ are shown in Figure 4.

In contrast to the 2-state telegraph model, the coordinate varies continuously over a range of q. The particle is found to spend the majority of the time in the left well, which has coordinate $q < 0$ and has lower potential energy, making occasional transitions to the right well, which has coordinate $q > 0$. Thus, the particle has longer residence times in the left well when compared with the right well. The autocorrelation function is biexponential, with a short time constant, $\tau_1 = 9.4$, arising from fluctuations within the potential energy wells and a longer time constant, $\tau_2 = 5{,}110$, arising from transitions between wells.

The simulation strategy was validated by comparing the rate constants obtained from the long time decay of the autocorrelation function to rate constants for passage over the barrier obtained from simulations of the reactive flux (15) and from theoretic estimates of the transition rate (16). In these approaches, $k = \kappa k_{TST}$, in which k is the sum of the forward and backward barrier crossing rate constants, k_{TST} is transition state theory estimate of the rate constant, and κ is the transmission coefficient. For compactness, the theoretic calculations are outlined in the appendix.

For the parameters given in Figure 4, $k_{TST} = 6.09 \times 10^{-4}$ and $\kappa = 0.33$; the transition rate is lower than that predicted by transition state theory due to slow spatial diffusion (SD) over the barrier. The resulting time constant $\tau = 1/k = 4{,}980$ agrees well with the fitted long time decay of the autocorrelation function, $\tau_2 = 5{,}110$. Figure 5 shows a more extensive comparison between the transmission coefficients obtained from theoretic estimates of the rate constant, the reactive flux method, and the

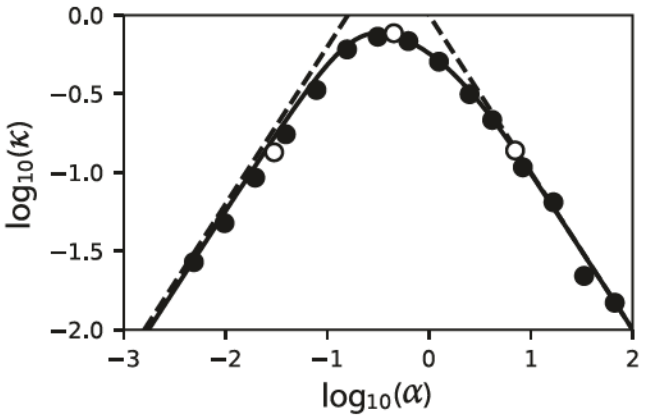

Fig 5. Barrier crossing transmission coefficients for the strong collision model. The simulations and calculations used $Q = 7$, $V_B = 2$, $\omega_A = \omega_B = 0.5$. Simulated transmission coefficients (solid circles) are obtained as $\kappa = 1/(\tau_c k_{TST})$ in which τ_c is the long time decay constant of the simulated autocorrelation function. Simulated transmission coefficients (open circles) are obtained from the reactive flux method (15). The solid curve shows the theoretic result and dashed lines show the limiting κ_{ED} and κ_{SD} transmission coefficients for the strong collision model, as described in the appendix.

long time decay of the simulated autocorrelation function.

The variation in the transmission coefficient displays the classic Kramers turnover. At low collision frequencies, the exchange rate increases in proportion to the collision frequency, while at high collision frequencies, the exchange rate decreases in proportion to the reciprocal of the collision frequency. At intermediate collision frequencies, the rate is a maximum, and the transition state theory provides a reasonable estimate of the exchange rate. Segments of the simulations for the strong collision model with $\alpha = 0.04$ and 2.5 are animated in Supplemental Movies S1 and S2. These parameters correspond to the energy dissipation (ED) and SD limits of the Kramers reaction rate theory discussed in the Appendix.

B. Comparison of continuous and discrete state frequency mappings

The telegraph signal $\omega(t)$ resulting from the mapping of the coordinate variable $q(t)$ to the frequency is shown in Figure 6a; the autocorrelation function is shown in Figure 6b. The telegraph signal only captures transitions between potential wells, and consequently, the autocorrelation function is monoexponential. The long time constant from the autocorrelation function of $q(t)$ and from the telegraph signal, $\tau_c = 5{,}110$, agree well, as expected. The spin relaxation rate constant is obtained, using Eq. 15, as the integral of the autocorrelation function; from the monoexponential fitting parameters, $R_{BWR} = <\delta\omega(t)^2>\tau_c = 1.96 \times 10^{-6}$. The real part of the complex NMR signal is shown in Figure 6c; the corresponding autocorrelation function is shown in Figure 6d. The relaxation rate constant obtained as the reciprocal of the decay time constant of the autocorrelation function is $R_{sc} = 1.90 \times 10^{-6}$, in good agreement with R_{BWR}. The agreement between these 2 results is consistent with the theoretic results previously mentioned. Empirically, the simulated autocorrelation function of the frequency fluctuations converges more rapidly than the simulated ensemble average NMR signal, as evident in the residual noise in Figure 6d. Thus, obtaining the relaxation rate constant from the autocorrelation function of the frequency fluctuations is more efficient in practice if the stochastic process is in the fast (BWR) limit.

A similar analysis was performed by using the random-coil model (vide supra). The results are shown in Figure 7. The function $\omega(t)$, obtained from $q(t)$, is shown in Figure 7a; the autocorrelation function is shown in Figure 7b. The autocorrelation function is biexponential, reflecting the fact that the model includes both fast fluctuations within potential wells and slower transitions between wells. The spin relaxation rate constant is obtained, using Eq. 15, as the integral of the autocorrelation function; for a biexponential autocorrelation function, $R_{BWR} = a_1\tau_1 + a_2\tau_2$, in which a_i and τ_i are the amplitude and time constant for the ith exponential term. From the biexponential fitting parameters, $R_{BWR} = 1.10 \times 10^{-6}$; the reduced relaxation rate constant, compared with the telegraph model, reflects the effect of the short time constant from the fast fluctuations with the potential well. The real part of the complex NMR signal is shown in Figure 7c; the corresponding autocorrelation function is shown in Figure 7d. The relaxation rate

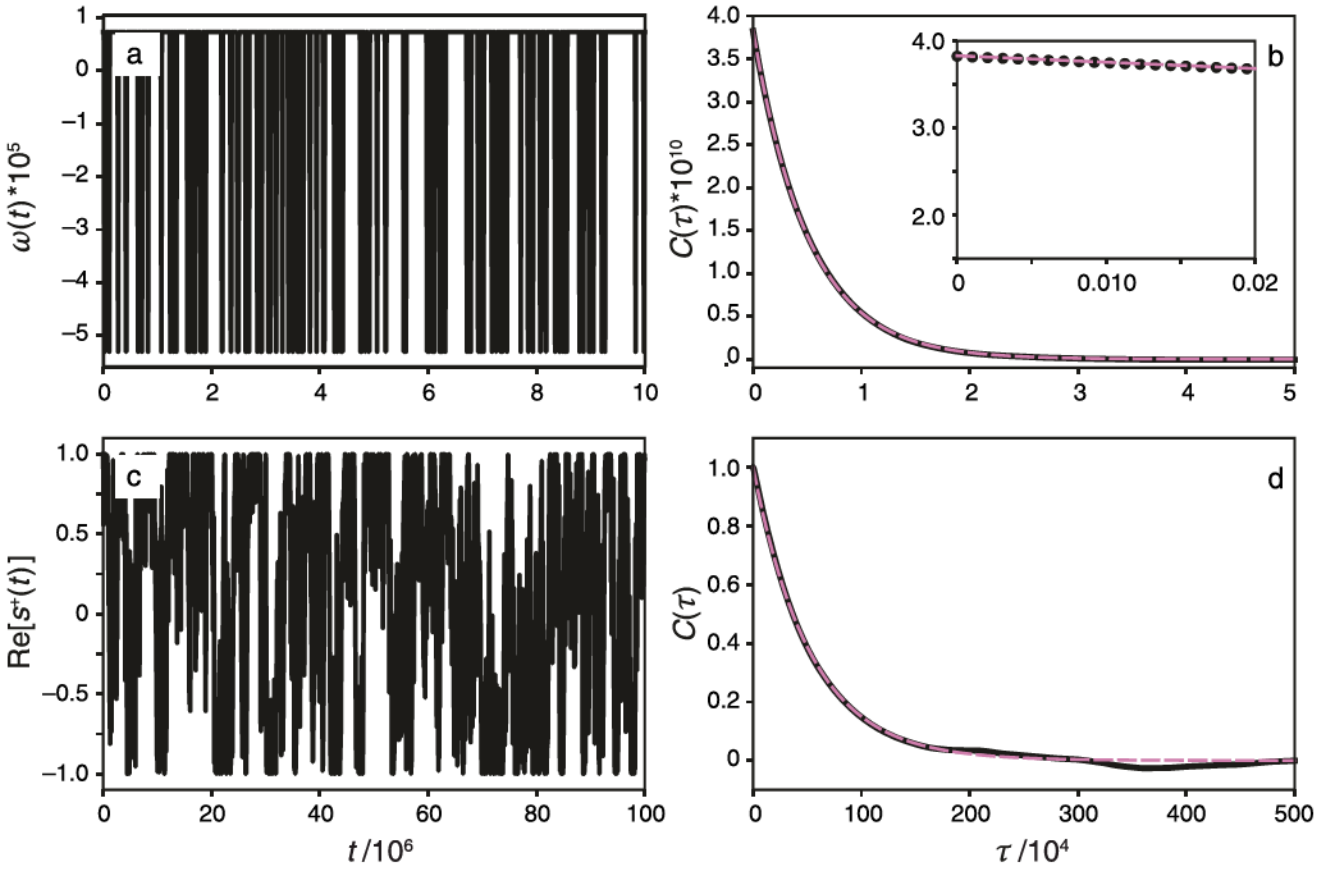

Fig 6. The 2-state telegraph model for dynamics in the biphasic potential with equal well frequencies. (a) Sample of $\omega(t)$ at times during the simulation with parameters chosen so $<\delta\omega(t)^2>^{1/2} = 1.96 \times 10^{-5}$. (b) Autocorrelation of $\omega(t)$ (black) fit with a monoexponential function (reddish–purple, dashed line) with amplitude $<\delta\omega(t)^2> = 3.83 \times 10^{-10}$ and decay time $\tau_c = 5110$; $<\delta\omega(t)^2>^{1/2}\tau_c = 0.1$ and an estimated value of $R_{BWR} = <\delta\omega(t)^2>\tau_c = 1.96 \times 10^{-6}$. The inset shows only a monoexponential decay. (c) Sample of Re[$s^+(t)$] at times during the simulation. (d) Real part of the autocorrelation of $s^+(t)$ (black) fit with a monoexponential function (reddish–purple, dashed line) with initial amplitude fixed at 1.0 and decay time constant of 5.27×10^5, yielding $R_{sc} = 1.90 \times 10^{-6}$ in good agreement with R_{BWR}. All parameters are dimensionless, as described in the text.

constant obtained as the reciprocal of the decay time constant of the autocorrelation function is $R_{sc} = 1.04 \times 10^{-6}$, in good agreement with R_{BWR}. Note that the autocorrelation of the NMR signal in Figure 7d is monoexponential, even when the autocorrelation function of $\omega(t)$ in Figure 7b is biexponential in the fast exchange limit, as described previously and illustrated in Figure 2.

A second simulation was performed for the parameters given in Figure 3 for the dashed curve: $Q = 7$, $V_B = 2$, $\omega_A = 0.5$, $\omega_B = 0.25$, and $\alpha = 2.5$, giving $k_{TST} = 3.41 \times 10^{-4}$ and $\kappa = 0.33$; the resulting long time constant $\tau = 1/k = 8{,}890$. Similar plots as for the previously mentioned model for the case of equal well frequencies are shown in Figures 8–10. The site populations are now $p_1 = 0.79$ and $p_2 = 0.21$. The long time decay constant of the autocorrelation function for $q(t)$, shown in Figure 8, is now $\tau_2 = 10{,}440$, in agreement with the theoretic result. Similar levels of agreement are found between R_{sc} and R_{BWR} for telegraph (Fig 9) and random-coil models (Fig 10) for the resonance frequencies. Notably, the autocorrelation function for the frequency fluctuations $\omega(t)$ in the random-coil model (Fig 10b) is distinctly biexponential, reflecting the effects of chemical shift averaging in the broader potential well for state 2. Again, the autocorrelation of the NMR signal in Figure 10d is monoexponential, even when the autocorrelation function of $\omega(t)$ is biexponential in the fast exchange limit.

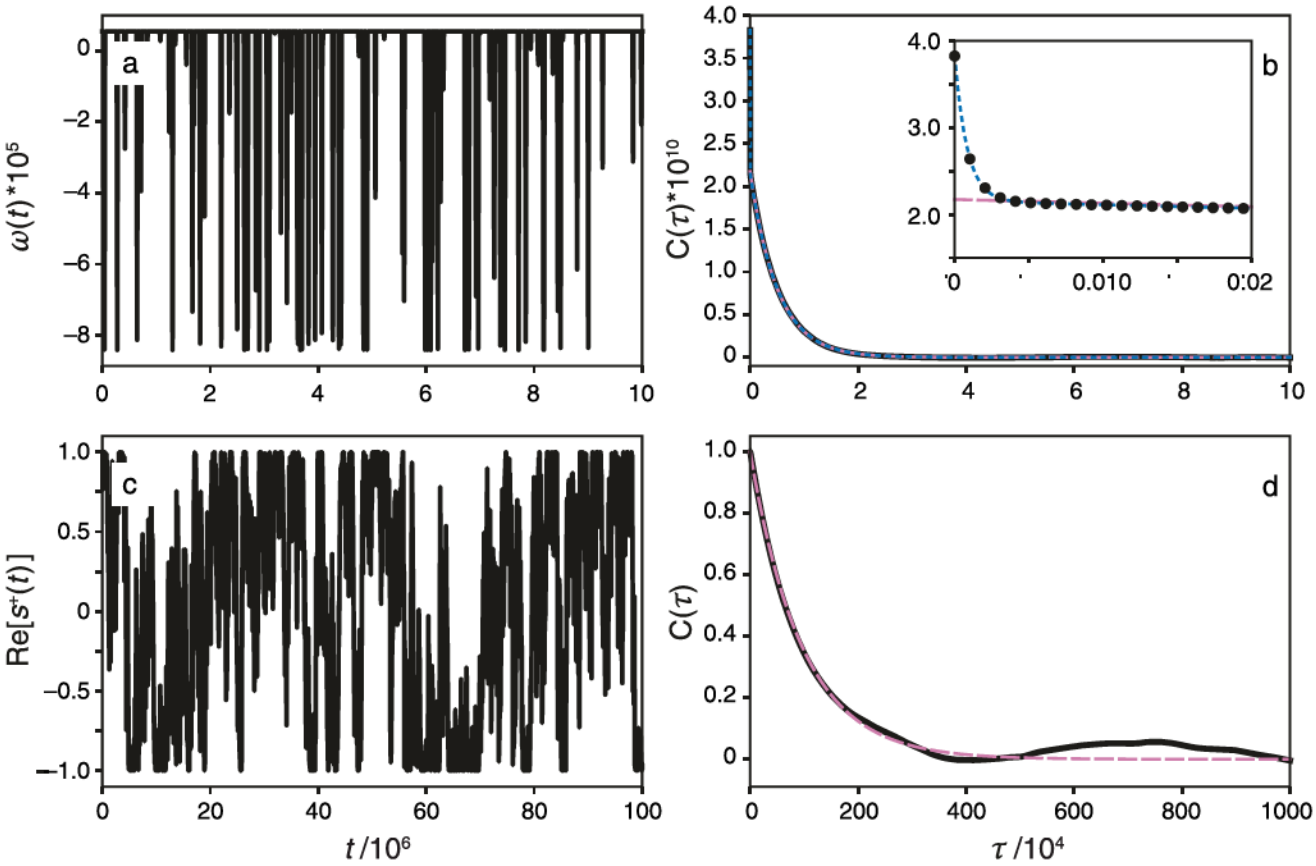

Fig 7. The 2-state random-coil model for the biphasic potential with equal well frequencies. (a) Sample of $\omega(t)$ at times during the simulation with parameters chosen, so $<\omega(t)^2>^{1/2} = 1.96 \times 10^{-5}$. (b) Autocorrelation of $\omega(t)$ (black) fit with monoexponential (reddish–purple, dashed line) and biexponential (blue, dotted line) functions. The inset shows the fast initial decay of the autocorrelation function, which is well described by the biexponential fit. The fitted parameters are amplitudes $a_1 = 1.67 \times 10^{-10}$ and $a_2 = 2.15 \times 10^{-10}$ and decay times $\tau_1 = 8.5$ and $\tau_2 = 5{,}110$; $<\delta\omega(t)^2>^{1/2}\tau_2 = 0.1$ and an estimated value of $R_{BWR} = 1.10 \times 10^{-6}$. (c) Sample of Re[$s^+(t)$] times during the simulation. (d) Real part of the autocorrelation of $s^+(t)$ (black) fit with a monoexponential (reddish–purple, dashed line) function with initial amplitude fixed at 1.0 and decay time constant of 9.60×10^5, yielding $R_{sc} = 1.04 \times 10^{-6}$ in good agreement with R_{BWR}. All parameters are dimensionless, as described in the text.

In simulations of both model potentials using the random-coil model for $\omega(t)$, the effect of averaging the chemical shift within the rightmost well (with higher minimum potential energy and consequently reduced population compared with the leftmost well) reduces the transverse relaxation rate constant by approximately a factor of 2. The result that fast timescale fluctuations of the resonance frequencies within the second well reduce, rather than increase, the transverse relaxation rate constant is a characteristic feature of the fast exchange regime in NMR spectroscopy. As the rates of frequency fluctuations become much larger than the range of frequencies sampled, the NMR transverse relaxation rate constant approaches 0, a process called motional narrowing (1).

C. CPMG relaxation dispersion for strong collision dynamics

CPMG relaxation dispersion was estimated by using the 2-state telegraph mapping of resonance frequencies applied to simulations by using the strong collision model in the asymmetric biphasic double-well potential (the dashed line in Fig 3) and $\tau_{cp} = 1.05 \times 10^4$ and 2.62×10^3. The ensemble signal $<s^+(t)>$ and the autocorrelation function of $s^+(t)$ are shown in Figure 11. The results show the effect of the CPMG pulse train as τ_{cp} is reduced. In the absence of the CPMG pulse train, the decay rate

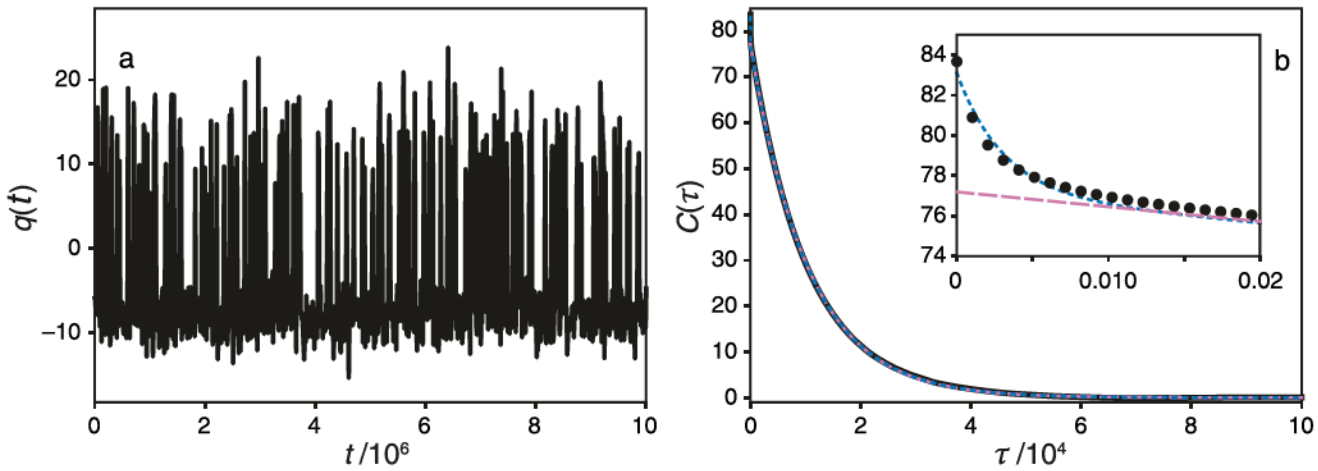

Fig 8. Strong collision model simulation of $q(t)$ for the biphasic potential with unequal well frequencies. Parameters were $Q = 7$, $V_B = 2$, $\omega_A = 0.5$, and $\omega_B = 0.25$ (dashed trace in Fig 2). The simulation used a time step of 0.01 and consisted of 2^{34} steps with a collision rate of $\alpha = 2.5$; $q(t)$ was stored every 2^{10} steps. (a) The $q(t)$ at every 1,000 stored sample point during the simulation. (b) Autocorrelation function of $q(t)$ (black) fit with a monoexponential (reddish–purple, dashed line) and biexponential (blue, dotted line) decay function; 10 replicate simulations were averaged to produce the final autocorrelation function. The inset shows the fast initial decay of the autocorrelation function, which is well described by the biexponential fit. The fitted parameters are amplitudes $a_1 = 6.0$ and $a_2 = 77.1$, and decay times $\tau_1 = 30.7$ and $\tau_2 = 10{,}440$. All parameters are dimensionless, as described in the text. The simulated dynamics in the potential are shown in Supplemental Movie S2.

is $\sim 9 \times 10^{-7}$ and drops to $\sim 2 \times 10^{-7}$ for $\tau_{cp} = 1.05 \times 10^4$ and to $\sim 2 \times 10^{-8}$ for $\tau_{cp} = 2.62 \times 10^3$.

An important aspect of CPMG experiments is illustrated by comparing relaxation dispersion curves acquired for the 2-state telegraph and random-coil mapping of resonance frequencies applied to simulations by using the strong collision model in the asymmetric biphasic double-well potential. The relaxation rate constants determined, as in Figure 11, are shown in Figure 12 for τ_{cp} values ranging from 327 to 4.19×10^4. The simulated data were fit by using Eq. 21, with an added constant offset. As can be seen in the inset to Figure 12, the offset is zero for the data using the 2-state model and positive for the random-coil model. The averaging of resonance frequencies in the well with $q(t) > 0$ gives rise to an initial fast decay of the autocorrelation function shown in Figure 10b, with a time constant of 32. This dynamic process is faster than the fastest pulsing used in the CPMG simulations ($\tau_{cp} = 327$), and consequently, the dephasing caused by this process cannot be refocused by the 180° pulses in the CPMG train. Instead, the plateau value represents the relaxation rate constant from dynamic processes faster than pulsing. Windowless CPMG and $R_{1\rho}$ experiments overcome this limitation and allow faster dynamic processes to be characterized (17–19).

V. DISCUSSION

Chemical exchange has emerged as one of the most powerful phenomena in NMR spectroscopy for investigating the conformational dynamics and chemical kinetics of biologic macromolecules (2). The present tutorial is intended to introduce chemical exchange dynamics and illustrate the connections between theoretic approaches conventionally used in NMR spectroscopy to model chemical exchange and chemical reaction rate theory in statistical mechanics.

A. Strong collision models for chemical exchange

A theoretic expression for the NMR signal was derived within the strong collision model and shown to be similar to expressions derived from conventional NMR approaches for chemical exchange (e.g., BWR theory or the random phase model). Numeric simulations of the dynamics were performed for a particle moving stochastically on a classical one-dimensional biphasic double-well potential by using the

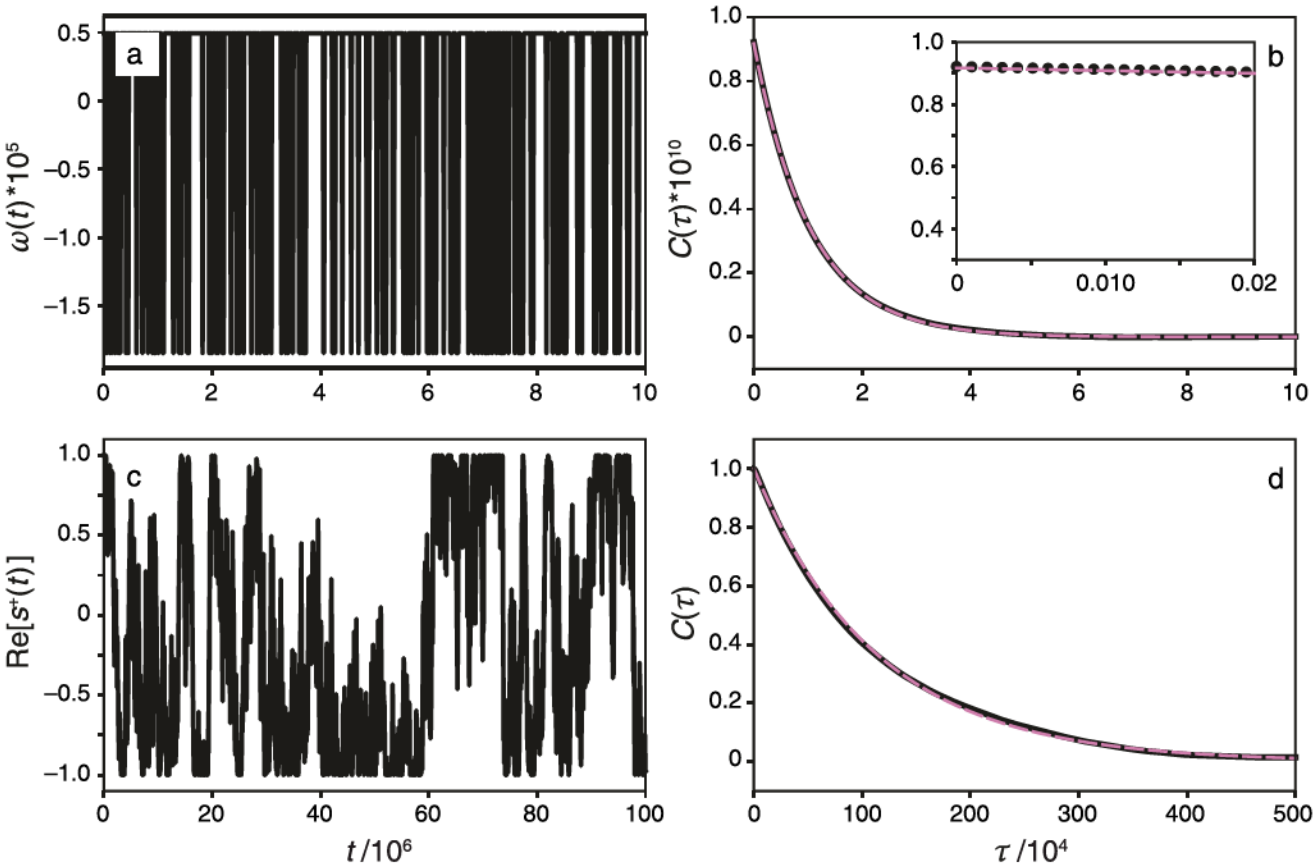

Fig 9. The 2-state telegraph model for the biphasic potential with unequal well frequencies. (a) Sample of $\omega(t)$ at times during the simulation with parameters chosen, so $<\delta\omega(t)^2>^{1/2} = 9.60 \times 10^{-6}$. (b) Autocorrelation of $\omega(t)$ (black) fit with a monoexponential function (reddish–purple, dashed line), with amplitude $<\delta\omega(t)^2> = 9.17 \times 10^{-11}$ and decay time $\tau_c = 10{,}440$; $<\delta\omega(t)^2>^{1/2}\tau_c = 0.1$ and an estimated value of $R_{BWR} = <\delta\omega(t)^2>\tau_c = 9.58 \times 10^{-7}$. The inset shows only the monoexponential decay. (c) Sample of Re[$s^+(t)$] at times during the simulation. (d) Real part of the autocorrelation of $s^+(t)$ (black) fit with a monoexponential (reddish–purple, dashed line) function with initial amplitude fixed at 1.0 and decay time constant of 1.13×10^6, yielding $R_{sc} = 8.83 \times 10^{-7}$ in good agreement with R_{BWR}. All parameters are dimensionless, as described in the text.

strong collision model. Simulations of dynamics of simple models provide ready access to the kinetic rate constants on the chemical exchange timescale (microsecond to millisecond), while capturing essential features of more complex molecular dynamics (e.g., macromolecules). Excellent agreement was obtained between the simulated rate constants for barrier crossing and the calculated rate constants on the basis of the formal statistical mechanical theory of kinetic processes.

The theoretic derivation of the NMR spin relaxation rate constant for chemical exchange is commonly obtained by using discrete state jump models for the underlying chemical dynamics. Such approaches conform well to the theoretic strong collision model, remembering that collisions have a somewhat different meaning in the 2 approaches. However, as is well known in statistical mechanics, a range of kinetic rate constants frequently can be obtained from simulations in either the strong collision model or the frictional "weak-collision" (Langevin) model, with the appropriate choice of parameters. In the weak-collision Langevin model, collisions are effectively continuous, each resulting in a change in the energy that is small compared with k_BT. Similar results to those presented for the strong collision model have been obtained by using Langevin dynamics (data not shown) (20, 21).

The simulations of a continuous variable model of dynamics in a biphasic double-well potential were mapped onto jump models for

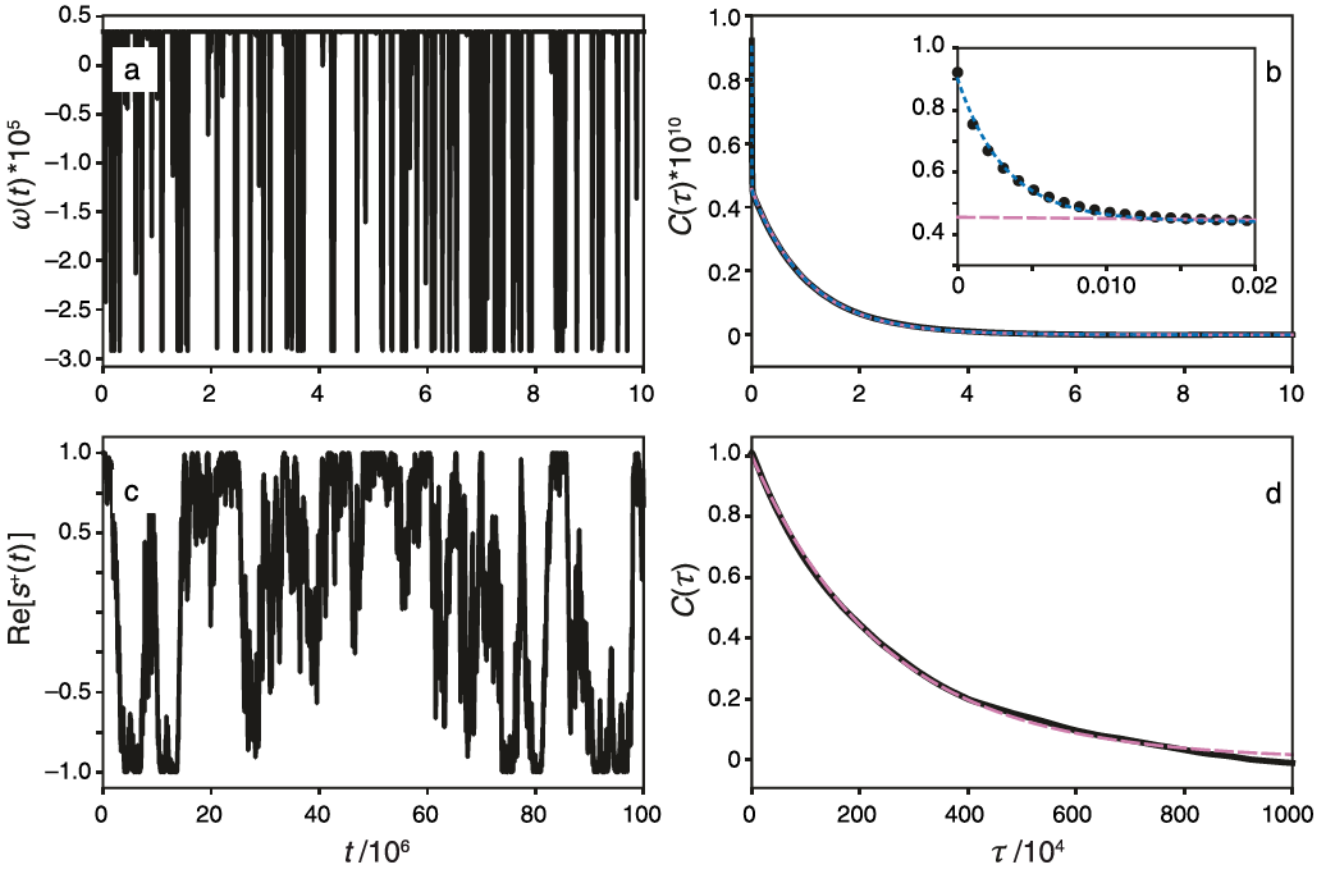

Fig 10. The 2-state random-coil model for the biphasic potential with unequal well frequencies. (a) Sample of $\omega(t)$ at times during the simulation with parameters chosen, so $<\omega(t)^2>^{1/2} = 9.60 \times 10^{-6}$. (b) Autocorrelation of $\omega(t)$ (black) fit with monoexponential (reddish–purple, dashed line) and biexponential (blue, dotted line) functions. The inset shows the fast initial decay of the autocorrelation function, which is well described by the biexponential fit. The fitted parameters are amplitudes $a_1 = 4.52 \times 10^{-11}$ and $a_2 = 4.49 \times 10^{-11}$ and decay times $\tau_1 = 32.0$ and $\tau_2 = 10{,}420$; $<\delta\omega(t)^2>^{1/2}\tau_2 = 0.1$ and an estimated value of $R_{BWR} = 4.69 \times 10^{-7}$. (c) Sample of Re[$s^+(t)$] at times during the simulation. (d) Real part of the autocorrelation of $s^+(t)$ (black) fit with a monoexponential (reddish–purple, dashed line) function with initial amplitude fixed at 1.0 and decay time constant of 2.47×10^6, yielding $R_{sc} = 4.05 \times 10^{-7}$ in good agreement with R_{BWR}. All parameters are dimensionless, as described in the text.

chemical exchange by defining discrete states for ranges of the position of the particle (for example, setting state 1 for $q < 0$ and state 2 for $q > 0$). The associated simulations were found to agree with theoretic results and can be used to explore the behavior of more complex models of chemical exchange, allowing for asymmetry between potential energy wells, as well as more complex mapping between the position of the particle and the NMR resonance frequency of a nuclear spin. These features mimic commonly occurring situations in which one "state" of a protein or other macromolecule is highly ordered, with limited stochastic variation in resonance frequencies, and the other state is highly disordered, with large stochastic variation in resonance frequencies.

The results of the theoretic derivations and numeric simulations have been presented in dimensionless units and can be rescaled to natural units, as desired by the choice of ω_1 and dimensional analysis. For example, the dimensionless value of the NMR relaxation rate constant $R_{sc} = 1.96 \times 10^{-6}$ is obtained from the telegraph signal model for the strong collision model with equal potential well frequencies (Fig 6). A choice of $\omega_1 = 1.0 \times 10^7$ s^{-1} then gives $R_{sc} = 19.6$ s^{-1}. The simulation used $<\delta\omega(t)^2>^{1/2}\tau_c = <\delta\omega(t)^2>^{1/2}/k_{ex} = 0.1$, so

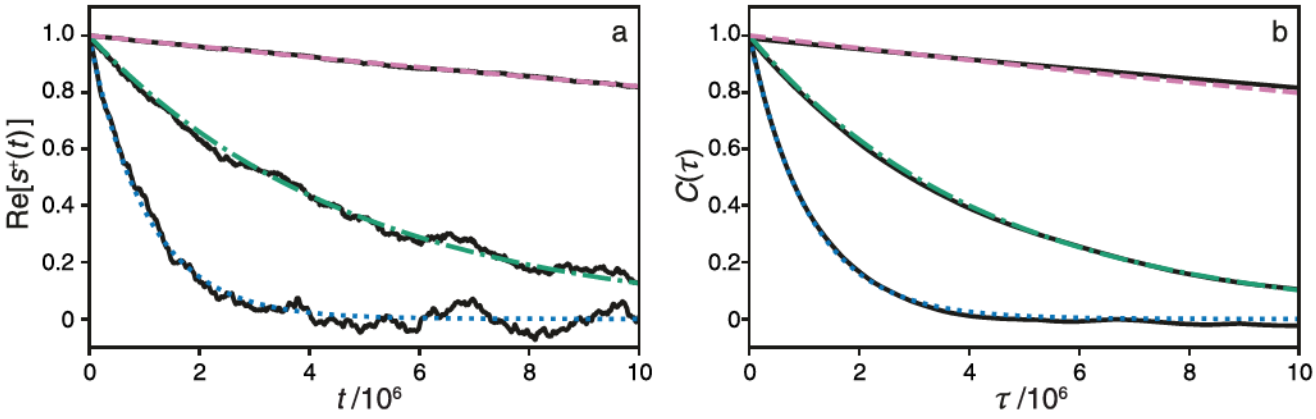

Fig 11. CPMG relaxation dispersion for the strong collision model, the biphasic potential with unequal well frequencies, and the telegraph signal mapping of resonance frequencies. Parameters were $Q = 7$, $V_B = 2$, $\omega_A = 0.5$, and $\omega_B = 0.25$ (dashed trace in Fig 3). The simulations used a time step of 0.01, and a collision rate of $\alpha = 2.5$; $q(t)$ was stored every 2^{10} steps. Values of τ_{cp} were 1.05×10^4 and 2.62×10^3. (a) Values of $s^+(t)$ for 640 trajectories of length 2^{29} steps were averaged to obtain $< s^+(t) >$. (b) Autocorrelation functions of $s^+(t)$ were calculated, as in Figure 8, for 20 individual trajectories of 2^{34} steps and averaged. In each figure, black lines are simulated results. Fits with single exponential functions are shown for absence of CPMG block (blue, dotted line), CPMG block with $\tau_{cp} = 1.05 \times 10^4$ (green, dash–dotted line), and CPMG block with $\tau_{cp} = 2.62 \times 10^3$ (reddish–purple, dashed line). The decay time constants in the absence of an applied CPMG pulse train agree well between the NMR signal and its autocorrelation function. The decay rates in the absence of the CPMG sequence are (a) 9.49×10^{-7} and (b) 9.16×10^{-7} (in good agreement with the results shown in Fig 8), the decay rates are (a) 2.07×10^{-7} and (b) 2.29×10^{-7} for $\tau_{cp} = 1.05 \times 10^4$, and the decay rates are (a) 1.97×10^{-8} and (b) 2.26×10^{-8} for $\tau_{cp} = 2.62 \times 10^3$.

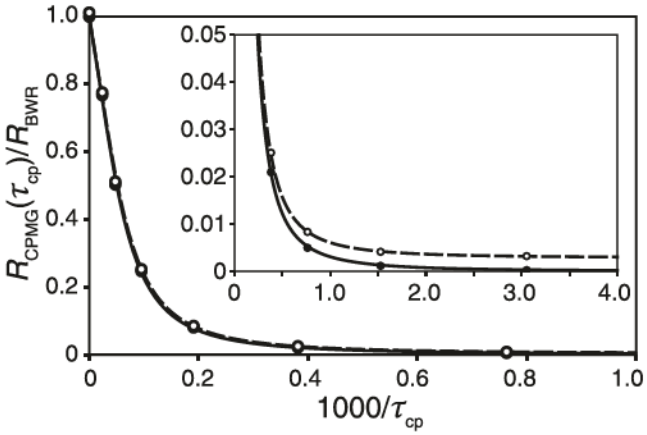

Fig 12. CPMG relaxation dispersion for 2-state (filled circles, solid line) and random-coil models (open circles, dashed line). Relaxation rate constants shown as circles were obtained as described in Figure 11. Simulated points were fit with Eq. 21 augmented by a constant offset parameter. Optimized values of $\tau_{ex} = 10{,}330$ and 10,200 for the telegraph and random-coil models, respectively, in agreement with the results shown in Figures 9 and 10. The optimized offset was 0 for the telegraph model and 1.36×10^{-9} for the random-coil model. The limiting relaxation rate constant for the random-coil model agrees well with the value of 1.44×10^{-9} obtained as the product of the amplitude and decay time for the fast component of the autocorrelation function shown in Figure 10b, confirming that the apparent plateau represents the contribution from dynamics processes faster than the CPMG pulsing rates. Data have been normalized by the relaxation rate constant in the absence of pulsing, R_{BWR}, for display.

from Eq. 14, and recalling $p_1 = 0.88$ and $p_2 = 0.12$ for the given potential, $k_{ex} = 1960\ s^{-1}$ and $\Delta\omega = 603\ s^{-1}$. These are values in the range typical of conformational changes in biologic macromolecules detected in actual NMR experiments (2).

The numeric simulations in the biphasic potential were performed for the most part by using parameters consistent with fast limit or BWR timescale chemical exchange for simplicity in comparing results to Eqs. 14 and 15. Extensive use was made of the autocorrelation functions of the resonance frequency fluctuations or of the NMR resonance frequency to obtain estimates of the transverse relaxation rate constant. As shown by Eq. 13 and results in Figure 2, the long time decay constant of the autocorrelation function is a good estimate of the relaxation rate constant outside of the fast limit. The actual range of application of Eq. 13 and related expressions for $R_{1\rho}$ and CPMG relaxation dispersion have been discussed elsewhere (2, 4, 5, 13). The simulations can be performed for stochastic processes on any timescale, and outside of the range of application of the autocorrelation function approach, the ensemble average free induction decay can

be modeled by summation of multiple independent simulations, in a similar fashion to the simulations represented in Figure 12a.

B. Further consideration of CMPG relaxation dispersion

The CPMG experiment is one of the most common and effective techniques used to assess exchange on the microsecond to millisecond timescale. The 180° pulses in the CPMG sequence have the effect of reversing the sense of precession of transverse magnetization and thus can be represented by inversion of the sign of the precession frequencies. In the present work, the effect of the CPMG pulse train was simulated by multiplying the NMR signal by a square wave function $sq[\pi t/(2\tau_{cp})]$ with period $4\tau_{cp}$ and varying between $+1$ and -1. As described in Figures 11 and 12, the simulated relaxation dispersion data provides an excellent fit to Eq. 21. As an alternative approach, Xue et al. have shown that the effective relaxation rate constant in a CPMG experiment can be obtained directly from the autocorrelation function of the frequency fluctuations, in a generalization of Eq. 15, also by multiplying by a square wave:

$$\begin{aligned} R_{CPMG}(\tau_{cp}) &= \int_0^\infty \langle \delta\omega(t) sq[\pi t/(2\tau_{cp})] \delta\omega(t+\tau) \\ &\qquad sq[\pi(t+\tau)/(2\tau_{cp})] \rangle d\tau \\ &= \int_0^\infty \langle \delta\omega(t)\delta\omega(t+\tau)\rangle \\ &\qquad \langle sq[\pi t/(2\tau_{cp})] sq\left[\pi(t+\tau)/(2\tau_{cp})\right]\rangle d\tau \\ &= \int_0^\infty \langle \delta\omega(t)\delta\omega(t+\tau)\rangle tri[\pi\tau/(2\tau_{cp})] d\tau \end{aligned} \tag{22}$$

in which $tri(x)$ is a triangle wave function that consists of linear segments connecting the extrema of the cosine function (10). The second equality of Eq. 22 is obtained because the fluctuations $\delta\omega(t)$ are uncorrelated with the time of applications of the 180° pulses, and the third line is obtained because the autocorrelation of the square wave function is the triangle wave function. Integration of the last line of Eq. 22 for $\langle \delta\omega(t)\delta\omega(t+\tau)\rangle = p_1 p_2 \Delta\omega^2 e^{-\tau/\tau_{ex}}$ yields Eq. 21. The integration can be performed by expanding $tri(x)$ in a Fourier cosine series, integrating each term in the Fourier series and summing the resulting series (22).

C. Generalization to dynamics in multiphasic many-well potentials

The 2-state kinetic model explored in this work exhibits the principal features of chemical exchange but also represents one of the most common scenarios encountered in experimental NMR spectroscopy. However, the simulation protocols developed as described previously for a 2-well biphasic potential are extendable to more complex kinetic schemes. As one example, a linear 3-site potential function (C–A–B) can be designed in a similar fashion as for the biphasic potential, as follows

$$V(q) = \begin{cases} V_B + \frac{1}{2} m\omega_B^2 (q - q_B)^2 & q > b \\ Q_{AB} - \frac{1}{2} m\omega_1^2 (q - q_{AB})^2 & b \geq q > a \\ \frac{1}{2} m\omega_A^2 q^2 & a \geq q > -c \\ Q_{AC} - \frac{1}{2} m\omega_1^2 (q + q_{AC})^2 & -c \geq q > -d \\ V_C + \frac{1}{2} m\omega_C^2 (q + q_C)^2 & q \leqslant -d \end{cases} \tag{23}$$

which includes parameters describing the 2 energy barrier heights (Q_{AC}, Q_{AB}), the energy difference between the main state and the 2 minor states (V_B, V_C), the positions of the minor state minima (q_B, q_C), the locations of the barriers (q_{AB}, q_{AC}), barrier transition frequencies (ω_1), the well frequencies (ω_A, ω_B, ω_C), and the mass (m). Eq. 23 is formulated with the position of the well A at $q = 0$. This potential also assumes for simplicity that the barrier frequencies are identical; the potential could be generalized to distinct barrier frequencies. The

potential function is made continuous by the following definitions:

$$
\begin{aligned}
a &= (m\omega_1^2 q_{AB}^2 - 2Q_{AB})/(m\omega_1^2 q_{AB}) \\
b &= \{2(Q_{AB} - V_B) - m\omega_1^2 q_{AB}(q_{AB} - q_B)\}/ \\
&\quad (m\omega_1^2(q_B - q_{AB}) \\
c &= (m\omega_1^2 q_{AC}^2 - 2Q_{AC})/(m\omega_1^2 q_{AC}) \\
d &= \{2(Q_{AC} - V_C) - m\omega_1^2 q_{AC}(q_{AC} - q_C)\}/ \\
&\quad (m\omega_1^2(q_C - q_{AC}) \\
\omega_A &= \omega_1\sqrt{(q_{AB} - a)/a} \\
\omega_B &= \omega_1\sqrt{(q_{AB} - b)/(b - q_B)} \\
\omega_C &= \omega_1\sqrt{(q_{AC} - d)/(d - q_C)}
\end{aligned}
\tag{24}
$$

Additionally, the A–C barrier location (q_{AC}) is constrained and is calculated by using the following equation:

$$q_{AC} = q_{AB}\sqrt{Q_{AC}/Q_{AB}} \tag{25}$$

Manipulation of the independent variables allows for the simulation of symmetric or asymmetric models with identical or distinct well frequencies. Strong collision dynamic simulations can then be performed similarly as for the biphasic potential model described. Theoretic results for N-site ($N > 2$) chemical exchange always can be computed numerically from the Bloch–McConnell equations, although approximate analytical solutions also are available for comparison with simulations (2). Efforts to parameterize Markov state models from molecular dynamics simulations, together with calculations of NMR chemical shifts from molecular structures, extend beyond the idealized 2- and 3-state models, given by Eqs. 16 and 23 (10, 11).

D. Other possible mappings of coordinates to resonance frequencies

The models presented previously can be modified or generalized by using other mappings between the particle position $q(t)$ and the spin resonance frequencies. A common justification for the application of the 2-site model in NMR spectroscopy relies on the assumption of rapid exchange between subsets of states. For example, if states 1 to M are in mutual fast exchange, and sites $M + 1$ to N are in mutual fast exchange, then the N-state system reduces to an effective 2-state system, with averaged site properties for the 2 sets of states. As noted by Trott and Palmer (23), convergence to this simplified 2-state result depends on all parameters of the spin system in a complex fashion. The random-coil model used herein tacitly assumed barrierless averaging of shifts to a mean of zero in the $q > 0$ state. Simulations in the 3-state potential, described previously, would allow for exploration of the convergence to a 2-state system by averaging of the states A and C, as the AC barrier is reduced relative to the AB barrier.

VI. CONCLUSION

The theoretic analysis and simulations presented previously are intended to illustrate the connection between the NMR phenomena of chemical exchange line broadening and nuclear spin relaxation and statistical mechanical chemical reaction rate theories of barrier crossing dynamics. In this work, we have attempted to show the value of the natural connections between the 2. The numeric simulations provide insights into how changes in NMR observables reflect the nature of the underlying state-to-state dynamics. This approach can be generalized to reflect specific features of the many and varied forms of biomolecular dynamics (11). Although most simulations were performed in the fast limit on the chemical shift timescale, the simulation methods themselves and the theoretic results derived have wider application; in particular, the theoretic results are generally accurate if the site populations are highly skewed (4, 13).

The numeric simulations using the strong collision model enabled comparison of results for the discrete state jump model (the telegraph model discussed previously) commonly used to analyze NMR chemical exchange measurements and a model in which resonance frequencies vary within a potential energy well (the random-coil model discussed

previously). The results, for example, comparing Figures 6 and 7 or Figures 9 and 10, show that chemical shift averaging within potential wells contributes to motional narrowing of resonance linewidths, compared with an assumed 2-state discrete jump. Thus, resonance linewidths or transverse relaxation rate constants are not interpretable in a simple manner because all NMR and kinetic parameters contribute to the observable quantity. In contrast, the CPMG relaxation dispersion curves shown in Figure 12 display nearly ideal discrete 2-state behavior even for the random-coil model. In many experimental situations, the fast-pulsing plateau value of $R_{CPMG}(\tau_{cp})$ is an adjustable parameter, and the offset for the random-coil model in Figure 12 would not be identified. Thus, the present results provide support for the use of discrete state models for analysis of relaxation dispersion measurements. However, chemical exchange processes faster than the maximum pulsing rate in CPMG experiments can be detected as anomalously large plateau values for $R_{CPMG}(\tau_{cp})$ or by $R_{1\rho}$ relaxation dispersion experiments. Such processes typically are attributed to presence of additional discrete chemical or conformational states. The present work raises the possibility that such effects could arise from conformational fluctuations within a potential energy basin.

Supplemental Material

Jupyter Notebook (Python 3.6) and Fortran 77 software used for strong collision simulations are available at: https://doi.org/10.35459/tbp.2021.000201.s1. Supplemental Movies 1 and 2 are available at: https://doi.org/10.35459/tbp.2021.000201.s2 and https://doi.org/10.35459/tbp.2021.000201.s3, respectively.

AUTHOR CONTRIBUTIONS

AGP and JES conceptualized and coordinated the project. All authors contributed to the theoretic developments, programming and simulations, and writing of the manuscript.

ACKNOWLEDGMENTS

This work began at the Telluride Science Research Center School on Biomolecular Structure and Dynamics: Theory and Experiment in 2017. The school was supported by the National Institutes of Health (NIH 1P41GM118302), National Science Foundation (NSF CHE-1362524), Boston University, Columbia University, and the New York Structural Biology Center. ND acknowledges support from a predoctoral fellowship from the Molecular Biophysics Training Grant (T32 GM008382). CN acknowledges support from the NIH (grant R01GM118792). MZ acknowledges support from the NSF (grant MCB-1616741, awarded to Jeffrey W. Peng). AGP acknowledges support from the NIH (grant R35 GM130398).

APPENDIX. CALCULATION OF REACTION RATE CONSTANTS FOR THE BIPHASIC POTENTIAL WITH STRONG COLLISION DYNAMICS

Extensive literature explores statistical mechanical theories for the absolute rate of barrier crossing (24). Transition state theory provides an upper bound for the rate of an activated barrier crossing. For a bistable potential with harmonic wells separated by a dimensionless barrier of height $Q >> 1$, the sum of the forward and reverse barrier crossing rate constants can be approximated as

$$k_{TST} = \frac{\omega_A}{2\pi} e^{-Q} + \frac{\omega_B}{2\pi} e^{-(Q - V_B)} \tag{A1}$$

This estimate of the rate constant assumes (a) an equilibrium population of states and (b) that an activated state will undergo a transition and be deactivated without recrossing of the barrier. The transition state theory rate constant is determined entirely by equilibrium properties of the system and has no dependence on collision rate, friction, or any aspect of system dynamics.

Transition state theory can be corrected by accounting for the role of barrier recrossing in reducing the rate constant below k_{TST}

$$k = \kappa k_{TST} \tag{A2}$$

in which k is the sum of the forward and reverse reaction rate constants and $\kappa \leq 1$ is the transmission coefficient. As was first recognized by Kramers (25), over a wide range of collision rate or friction, the transmission coefficient shows a turnover between the energy diffusion regime (of low collision rate or low friction), where barrier recrossings occur due to inertial effects and slow ED, and the SD regime (of high collision rate or high friction), where barrier recrossings occur due to slow SD over the barrier (26).

For the strong collision model, a transmission coefficient κ valid for all collision rate regimes has been derived by Berezhkovskii et al. (16)

$$k = \kappa_l \kappa_h \tag{A3}$$

in which κ_l and κ_h are the transmission coefficients in the low to intermediate and intermediate to high collision rate regimes, respectively. In the low to intermediate collision rate regime, the transmission coefficient is given by

$$\kappa_l = \int_0^\infty \frac{\left(1 - e^{-\alpha T_A(\varepsilon)}\right)\left(1 - e^{-\alpha T_B(\varepsilon)}\right)}{1 - e^{-\alpha\left(T_A(\varepsilon) + T_B(\varepsilon)\right)}} e^{-\varepsilon} d\varepsilon \tag{A4}$$

In the absence of collisions, the time period $T_A(\varepsilon)$ for a particle

located initially at $q = 0$ with kinetic energy ε and velocity < 0 to return to $q = 0$ with kinetic energy ε and velocity > 0 and the time period $T_B(\varepsilon)$ for a particle located initially at $q = 0$ with kinetic energy ε and velocity > 0 to return to $q = 0$ with kinetic energy ε and velocity < 0 are given by

$$T_A(\varepsilon) = 2\int_{q_{\min}(\varepsilon)}^{0} \frac{dq}{\sqrt{\varepsilon + Q - V(q)}}$$
$$T_B(\varepsilon) = 2\int_{0}^{q_{\max}(\varepsilon)} \frac{dq}{\sqrt{\varepsilon + Q - V_B - V(q)}} \quad \text{(A5)}$$

in which $q_{\min}(\varepsilon)$ and $q_{\max}(\varepsilon)$ are the classical turning points in the potential. Each of these integrals leads to a similar functional form

$$T_X(\varepsilon) = \frac{2\pi}{\omega_X}\left\{1 - \frac{1}{\pi}\tan^{-1}\sqrt{U_X^2\omega_X^2 + \varepsilon U_X(1+\omega_X^2)}\right\} + \frac{1}{2}\cosh^{-1}\left(\frac{U_X\omega_X^2}{\varepsilon(1+\omega_X^2)} + 1\right) \quad \text{(A6)}$$

in which $X = \{A, B\}$ and $U_X = \{Q, Q - V_B\}$. The energy diffusion regime is reached as $\alpha \to 0$. For well frequencies similar to the barrier frequency, i.e., $0.25 \le \omega_X \le 1.5$, $\kappa_I = \kappa_{ED} = 2\pi\alpha/(\omega_A + \omega_B)$. In the intermediate to high collision rate regime, the transmission coefficient is given by

$$\kappa_h = \int_0^\infty e^{-z}\tanh(z/\alpha)dz \quad \text{(A7)}$$

As $\alpha \to \infty$, the SD regime is reached, and $\kappa_h = \kappa_{SD} = 1/\alpha$ (in dimensionless units).

REFERENCES

1. Cavanagh, J., W. J. Fairbrother, A. G. Palmer, M. Rance, and N. J. Skelton. 2007. Protein NMR Spectroscopy: Principles and Practice. Academic Press, San Diego.
2. Palmer, A. G., and H. Koss. 2019. Chemical exchange. *Methods Enzymol* 615:177–236.
3. Sekhar, A., and L. E. Kay. 2019. An NMR view of protein dynamics in health and disease. *Annu Rev Biophys* 48:297–319.
4. Abergel, D., and A. G. Palmer. 2003. On the use of the stochastic Liouville equation in NMR: application to $R_{1\rho}$ relaxation in the presence of exchange. *Concepts Magn Reson* 19A:134–148.
5. Abergel, D., and A. G. Palmer. 2005. A Markov model for relaxation and exchange in NMR spectroscopy. *J Phys Chem B* 109:4837–4844.
6. Trott, O., D. Abergel, and A. G. Palmer. 2003. An average-magnetization analysis of $R_{1\rho}$ relaxation outside the fast-exchange limit. *Mol Phys* 101:753–763.
7. Schurr, J. M., B. S. Fujimoto, R. Diaz, and B. H. Robinson. 1999. Manifestations of slow site exchange processes in solution NMR: a continuous Gaussian exchange model. *J Magn Reson* 140:404–431.
8. Montgomery, J. A., Jr., D. Chandler, and B. J. Berne. 1979. Trajectory analysis of a kinetic theory for isomerization dynamics in condensed phases. *J Chem Phys* 70:4056–4066.
9. Straub, J. E., M. Borkovec, and B. J. Berne. 1987. Calculation of dynamic friction on intramolecular degrees of freedom. *J Phys Chem* 91:4995–4998.
10. Xue, Y., J. M. Ward, T. Yuwen, I. S. Podkorytov, and N. R. Skrynnikov. 2012. Microsecond time-scale conformational exchange in proteins: using long molecular dynamics trajectory to simulate NMR relaxation dispersion data. *J Am Chem Soc* 134:2555–2562.
11. Olsson, S., and F. Noé. 2017. Mechanistic models of chemical exchange induced relaxation in protein NMR. *J Am Chem Soc* 139:200–210.
12. Goldman, M. 1995. A simple formalism for the analysis of NMR in the presence of exchange. *Mol Phys* 86:301–315.
13. Abergel, D., and A. G. Palmer. 2004. Approximate solutions of the Bloch–McConnell equations for two-site chemical exchange. *ChemPhysChem*. 5:787–793.
14. Goldman, M., T. Tabti, C. Fermon, J. F. Jacquinot, and G. Saux. 1993. A model for the influence of motion on the NMR lineshape. *J Magn Reson A* 103:288–296.
15. Berne, B. J., M. Borkovec, and J. E. Straub. 1988. Classical and modern methods in reaction rate theory. *J Chem Phys* 92:3711–3725.
16. Berezhkovskii, A. M., D. J. Bicout, and G. H. Weiss. 1999. Collision model for activated rate processes: turnover behavior of the rate constant. *J Chem Phys* 11:11050–11059.
17. Ban, D., A. D. Gossert, K. Giller, S. Becker, C. Griesinger, and D. Lee. 2012. Exceeding the limit of dynamics studies on biomolecules using high spin-lock field strengths with a cryogenically cooled probehead. *J Magn Reson* 221:1–4.
18. Ban, D., A. Mazur, M. G. Carneiro, T. M. Sabo, K. Giller, L. M. Koharudin, S. Becker, A. M. Gronenborn, C. Griesinger, and D. Lee. 2013. Enhanced accuracy of kinetic information from CT-CPMG experiments by transverse rotating-frame spectroscopy. *J Biomol NMR* 57:73–82.
19. Reddy, J. G., S. Pratihar, D. Ban, S. Frischkorn, S. Becker, C. Griesinger, and D. Lee. 2018. Simultaneous determination of fast and slow dynamics in molecules using extreme CPMG relaxation dispersion experiments. *J Biomol NMR* 70:1–9.
20. Grønbech-Jensen, N., and O. Farago. 2013. A simple and effective Verlet-type algorithm for simulating Langevin dynamics. *Mol Phys* 111:983–991.
21. Jensen, L. F. G., and N. Grønbech-Jensen. 2019. Accurate configurational and kinetic statistics in discrete-time Langevin systems. *Mol Phys* 117:2511–2526.
22. Straub, J. 2020. Mathematical Methods for Molecular Science. Unit Circle Press, Cambridge, MA.
23. Trott, O., and A. G. Palmer. 2004. Theoretical study of $R_{1\rho}$ rotating-frame and R_2 free-precession relaxation in the presence of *n*-site chemical exchange. *J Magn Reson A* 170:104–112.
24. Hänggi, P., P. Talkner, and M. Borkovec. 1990. Reaction-rate theory: fifty years after Kramers. *Rev Mod Phys* 62:251–341.
25. Kramers, H. A. 1940. Brownian motion in a field of force and the diffusion model of chemical reactions. *Physica* 7:284–304.
26. Frauenfelder, H., and P. G. Wolynes. 1985. Rate theories and puzzles of hemeprotein kinetics. *Science* 229:337–345.